Do surface lateral flows matter for data assimilation of soil moisture observations into hyperresolution land models?

Running title: HYPERRESOLUTION LAND DATA ASSIMILATION

Yohei Sawada[1],

[1] Meteorological Research Institute, Japan Meteorological Agency, Tsukuba, Japan

Corresponding author: Y. Sawada, Meteorological Research Institute, Japan Meteorological Agency, 1-1, Nagamine, Tsukuba, Japan, ysawada@mri-jma.go.jp

This article is a non-peer reviewed preprint published at EarthArXiv

Key Points:

1. Surface lateral flows matter when soil moisture observations are assimilated into high-resolution integrated surface-groundwater land models.
2. The non-Gaussianity of the background error induced by the nonlinear dynamics of topography-driven surface flows harms the performance of an ensemble Kalman filter.

Keywords: data assimilation, hyperresolution land model, soil moisture

Abstract

Hyperresolution land modeling is expected to innovate the simulation of terrestrial water, energy, and carbon cycles. One of the major advantages of existing hyperresolution land models against conventional 1-demensional land surface models is that surface and subsurface lateral water flows can be explicitly simulated. Despite a lot of efforts on assimilating hydrological observations into the hyperresolution integrated surface-groundwater land models, how and in what case topography-driven surface water flows matter for data assimilation of soil moisture observations has yet to be clarified. In this study, I perform a minimalist synthetic numerical experiment, in which shallow soil moisture observations are assimilated into an integrated surface-groundwater land model by the ensemble Kalman filter. Propagation of a background error due to surface lateral water flows is crucially important to adjust the unobserved model state and parameter variables by horizontally propagating the information of soil moisture observations. However, the non-Gaussianity of the background error induced by the nonlinear dynamics of topography-driven surface flows harms the performance of an ensemble Kalman filter. It is difficult to efficiently constrain model states at the edge of the area where topography-driven surface flows reach by linear-Gaussian filters, which brings the new challenge in land data assimilation for hyperresolution land models. The new capability of data assimilation with the hyperresolution land models found in this study may improve the monitoring and prediction of flash floods caused by local severe rainfalls.

1. Introduction

Hyperresolution land modeling is expected to innovate the simulation of terrestrial water, energy, and carbon cycles, which is crucially important for meteorological, hydrological and ecological applications (see Wood et al. (2011) for the comprehensive review). While conventional land surface models (LSMs) assume that lateral water flows are negligible at a coarse resolution and solve vertical 1-demensional Richards equation for the soil moisture simulation (e.g., Sellers et al. 1996; Lawrence et al. 2011), currently proposed hyperresolution land models, which can be applied at a finer resolution (<1km), explicitly consider surface and subsurface lateral water flows (e.g., Maxwell and Miller 2005; Tian et al. 2012; Shrestha et al. 2014; Niu et al. 2014). Previous works indicated that a lateral transport of water plays important roles in terrestrial water and energy cycles (e.g., Maxwell and Condon 2016; Ji et al. 2017; Fang et al. 2017) and land-atmosphere interactions (e.g., Williams and Maxwell 2011; Keune et al. 2016).

Data assimilation has contributed to improving the performance of LSMs by fusing simulation and observation. The grand challenge of land data assimilation is to estimate unobservable variables from observations by propagating observations' information into model's high dimensional state and parameter space. In previous works on the conventional 1-D LSMs, many land data assimilation systems (LDASs) have been proposed to accurately estimate model's state and parameter variables, which cannot be directly observed, by assimilating satellite and in-situ observations. For example, the optimization of LSM's unknown parameters (e.g., hydraulic conductivity) has been implemented by assimilating remotely sensed microwave observations (e.g., Yang et al. 2007; Yang et al. 2009; Bandara et al. 2014; Bandara et al. 2015; Sawada and Koike 2014; Han et al. 2014). Kumar et al. (2009) analyzed the simulated correlation between surface soil moisture and root-zone soil moisture to improve the simulation of root-zone soil moisture by assimilating remotely sensed surface soil moisture observations. Sawada et al. (2015) successfully improved the simulation of root-zone soil moisture by assimilating microwave brightness temperature observations which include the information of vegetation water content. Gravity Recovery and Climate Experiment total water storage observation has been intensively used to improve the simulation of groundwater and soil moisture (e.g., Li et al. 2012; Houborg et al. 2012). Improving the simulation of state variables such as soil moisture and biomass by LDASs has contributed to accurately estimating fluxes such as evapotranspiration (e.g. Martens et al. 2017) and CO_2 flux (e.g., Verbeeck et al. 2011). However, in most of the studies on the conventional 1-D LDASs, observations impacted state and parameter variables only in a single model's horizontal grid which is identical to the location of the observation. The assumption that the surface and subsurface water flows are restricted to vertical direction in LSMs makes it difficult to propagate observation’s information horizontally, which limits the potential of land data assimilation to fully use land hydrological observations.

The hyperresolution land models, which explicitly solve surface and subsurface lateral flows, provide a unique opportunity to examine the potential of land data assimilation to propagate observation’s information horizontally in a model space and efficiently use land hydrological observations. Previous works successfully applied Ensemble Kalman Filters (EnKF) to 3-D Richards’ equation-based integrated surface-groundwater models. For example, Camporese et al. (2009) and Camporese et al. (2010) successfully assimilated the synthetic observations of surface pressure head and streamflow into the Catchment Hydrology (CATHY). Kurtz et al. (2016) coupled the Parallel Data Assimilation Framework (PDAF) (Nerger and Hiller 2013) with the Terrestrial System Modelling Framework (TerrSysMP) (Shrestha et al. 2014). The performance of TerrSysMP-PDAF to assimilate soil moisture observations was evaluated by a simple synthetic experiment (see also Zhang et al. (2018)).

Although the data assimilation of hydrological observations into the hyperresolution land models has been successfully implemented in the synthetic experiments, it is unclear how and in what case topography-driven surface lateral water flows matter for data assimilation of soil moisture observations. Previous studies on data assimilation with high resolution models mainly focused on assimilating groundwater observations (e.g., Ait-El-Fquih et al. 2016; Rasmussen et al. 2015; Hendricks-Franssen et al. 2008). There are some applications which focused on the observation of soil moisture and pressure head in shallow unsaturated soil layers. However, in those literatures, topography-driven surface flows have not been considered in the experiment (Kurtz et al. 2016) or the role of them in assimilating observations into the hyperresolution land models has not been quantitatively discussed (Camporese et al. 2010; Camporese et al. 2009). This study aims at clarifying if surface lateral flows matter for data assimilation of soil moisture observations into hyperresolution land models by a minimalist numerical experiment.

2. Methods

2.1. Model

ParFlow is an open source platform which realizes fully integrated surface-groundwater flow modeling (Kollet and Maxwell 2006; Maxwell et al. 2015). This parallel simulation platform has been widely used as a core hydrological module in hyperresolution land models (e.g., Maxwell and Kollet 2008; Maxwell and Condon 2016; Fang et al. 2017; Kurtz et al. 2016; Maxwell et al. 2011; Williams and Maxwell 2011; Shrestha et al. 2014). The brief description on the method of ParFlow to simulate integrated surface-subsurface water flows can be found below and the complete description of ParFlow can be found in Kollet and Maxwell (2006), Maxwell et al. (2015) and references therein.

In the subsurface, ParFlow solves the variably saturated Richards equation in three dimensions.

$$S_S S_W(h)\frac{\partial h}{\partial t} + \phi S_W(h)\frac{\partial S_W(h)}{\partial t} = \nabla \cdot \mathbf{q} + q_r \quad (1)$$

$$\mathbf{q} = -\boldsymbol{K_s}(\boldsymbol{x})k_r(h)[\nabla(h+z)cos\theta_x + sin\theta_x] \quad (2)$$

In equation (1), h is the pressure head [L]; z is the elevation with the z axis specified as upward [L]; S_S is the specific storage [L^{-1}]; S_W is the relative saturation; ϕ is the porosity [-]; q_r is a general source/sink term. Equation (2) describes the flux term $\mathbf{q}$ [LT^{-1}] based on Darcy's law, and $\boldsymbol{K_s}$ is the saturated hydraulic conductivity tensor [LT^{-1}]; k_r is the relative permeability [-]; θ is the local angle of topographic slope (see Maxwell et al. 2015). In this paper, the saturated hydraulic conductivity is assumed to be isotropic and the function of z:

$$\boldsymbol{K_s} = K_s(z) = K_{s,surface}\exp(-f(z_{surface} - z)) \quad (3)$$

where $K_{s,surface}$ is the saturated hydraulic conductivity at the soil surface, and $z_{surface}$ is the elevation of the soil surface. The saturated hydraulic conductivity decreases exponentially as the soil depth increases (Beven 1982). The van Genuchten relationship (van Genuchten 1980) is used to describe the relative saturation and permeability functions.

Overland flow is solved by the two-dimensional kinematic wave equation. The dynamics of the surface ponding depth, h [L], can be described by:

$$\mathbf{k} \cdot [-K_s(z)k_r(h) \cdot \nabla(h+z)] = \frac{\partial \|h,0\|}{\partial t} - \nabla \cdot \|h,0\|\boldsymbol{v_{sw}} + q_r \quad (4)$$

In equation (4), $\mathbf{k}$ is the unit vector in the vertical and $\|a,b\|$ indicates the greater value of the two quantities following the notation of Maxwell et al. (2015). If h < 0, equation

(4) describes that vertical fluxes across the land surface boundary is equal to a general source/sink term q_r (i.e., rainfall and evapotranspiration). If h > 0, the terms on the right-hand side of equation (4), which indicates water fluxes routed according to surface topography, are active. $\boldsymbol{v_{sw}}$ is the two-dimensional depth-averaged overland flow velocity [LT^{-1}] and estimated by the Manning's law:

$$\boldsymbol{v_{sw}} = \begin{pmatrix} \frac{\sqrt{S_{f,x}}}{n} h^{\frac{2}{3}} \\ \frac{\sqrt{S_{f,y}}}{n} h^{\frac{2}{3}} \end{pmatrix} \quad (5)$$

where $S_{f,x}$ and $S_{f,y}$ are the friction slopes [-] for the x- and y-direction, respectively; n is the Manning's coefficient [$TL^{-1/3}$]. In the kinematic wave approximation, the friction slopes are set to the bed slopes. The methodology of discretization and numerical implementation to solve equations (1-5) can be found in Kollet and Maxwell (2006).

2.2. Data Assimilation

In this paper, the ensemble Kalman filter (EnKF) was applied to assimilate soil moisture observations into ParFlow. The general description of the Kalman filter is the following:

$$\boldsymbol{x}^f(t) = \mathcal{M}[\boldsymbol{x}^a(t-1)] \quad (6)$$

$$\boldsymbol{x}^a(t) = \boldsymbol{x}^f(t) + \boldsymbol{K}[y^o - \mathcal{H}\boldsymbol{x}^f(t)] \quad (7)$$

$$\mathbf{K} = \boldsymbol{P}^f \boldsymbol{\mathcal{H}}^{\boldsymbol{T}} (\boldsymbol{\mathcal{H}} \boldsymbol{P}^{\boldsymbol{f}} \boldsymbol{\mathcal{H}}^{\boldsymbol{T}} + \boldsymbol{R})^{-\mathbf{1}} \quad (8)$$

$$\boldsymbol{P}^{\boldsymbol{a}} = (\boldsymbol{I} - \boldsymbol{K}\boldsymbol{\mathcal{H}})\boldsymbol{P}^{\boldsymbol{f}} \quad (9)$$

I follow the notation of Houtekamer and Zhang (2016). In equation (6), a forecast model $\mathcal{M}$ (ParFlow in this study) is used to obtain a prior estimate at time t, $\boldsymbol{x}^f(t)$, from the estimation at the previous time $\boldsymbol{x}^a(t-1)$. In equation (7), a prior estimate $\boldsymbol{x}^f(t)$ is updated to the analysis state, $\boldsymbol{x}^a(t)$, using new observations y^o. The Kalman gain matrix **K** calculated by equation (8) is used to give an appropriate weight between the observations with an error covariance matrix $\boldsymbol{R}$, and the prior with an error covariance matrix $\boldsymbol{P}^f$. To calculate **K**, the observation operator $\boldsymbol{\mathcal{H}}$ is needed to map from model space to observation space. It should be noted that the equations (6-9) give an optimal estimation only when the error in model and observation follows the Gaussian distribution. When the probabilistic distribution of the error in either model or observation has non-Gaussian structure, results of the Kalman filter are suboptimal. This point is important to interpret the results of this study.

EnKF is the Monte Carlo implementation of equations (6-9). To compute the Kalman gain matrix, **K,** ensemble approximations of $\boldsymbol{P}^f \boldsymbol{\mathcal{H}}^{\boldsymbol{T}}$ and $\boldsymbol{\mathcal{H}} \boldsymbol{P}^{\boldsymbol{f}} \boldsymbol{\mathcal{H}}^{\boldsymbol{T}}$ can be given by:

$$\boldsymbol{P^f \mathcal{H}^T} \equiv \frac{1}{k-1}\sum_{i=1}^{k}\left(x_i^f - \overline{x^f}\right)\left(\mathcal{H}x_i^f - \overline{\mathcal{H}x^f}\right)^T \quad (10)$$

$$\boldsymbol{\mathcal{H} P^f \mathcal{H}^T} \equiv \frac{1}{k-1}\sum_{i=1}^{k}\left(\mathcal{H}x_i^f - \overline{\mathcal{H}x^f}\right)\left(\mathcal{H}x_i^f - \overline{\mathcal{H}x^f}\right)^T \quad (11)$$

where x_i^f is the ith member of a k-member ensemble prior and $\overline{x^f} = \frac{1}{k}\sum_{i=1}^{k} x_i^f$ and $\overline{\mathcal{H}x^f} = \frac{1}{k}\sum_{i=1}^{k}\mathcal{H}x_i^f$.

Once $\overline{x^a} = \sum_{i=1}^{k} x_i^a$ (x_i^a is the ith member of a k-member ensemble analysis) and $\boldsymbol{P^a} = \boldsymbol{\frac{1}{k-1}}\sum_{i=1}^{k}(x_i^a - \overline{x^a})(x_i^a - \overline{x^a})^T$ are computed by equations (6-11), there are still many possible choices of an analysis ensemble. There are many proposed flavors of EnKF and one of the main differences among them is how to choose the analysis ensemble x_i^a. In this paper, the Ensemble Transform Kalman Filter (ETKF; Bishop et al. 2001; Hunt et al. 2007) was used to transport forecast ensembles to analysis ensembles.

In the ETKF, the analysis update for an ensemble mean is done by the following equations:

$$\tilde{P}^a = [(k-1)I + (Y^f)^T R^{-1} Y^f]^{-1} \quad (12)$$

$$\overline{w}^a = \tilde{P}^a (Y^f)^T R^{-1}(y^o - \overline{y^f}) \quad (13)$$

$$\overline{x^a} = \overline{x^f} + X^f \overline{w}^a \quad (14)$$

where the ith columns of Y^f and X^f are $y_i^f - \overline{y^f}$ and $x_i^f - \overline{x^f}$, respectively. y_i^f is defined by $y_i^f = \mathcal{H}x_i^f$ and $\overline{y^f}$ is the ensemble mean of y_i^f. I is the identity matrix.

The analysis covariance $\boldsymbol{P^a}$ is given by:

$$P^a = \frac{1}{k-1} X^a (X^a)^T = X^f \tilde{P}^a (X^f)^T \quad (15)$$

where the ith column of X^a is $x_i^a - \overline{x^a}$. The perturbations of the analysis ensemble members can be generated by the square root of $\tilde{P}^a$:

$$W^a = [(k-1)\tilde{P}^a]^{1/2} \quad (16)$$

$$X^a = X^f W^a \quad (17)$$

Please refer to Hunt et al. (2007) for the complete description of the ETKF and its localized version, the Local Ensemble Transform Kalman Filter (LETKF).

In many ensemble Kalman filter systems, the ensemble spread tends to become underdispersive without any ensemble inflation methods (Houtekamer and Zhang, 2016). In this paper, the relaxation to prior perturbation method (RTPP) of Zhang et al. (2004) was used to maintain an appropriate ensemble spread. In the RTPP, the computed analysis perturbations are relaxed back to the forecast perturbations:

$$x_{i,new}^{a} = (1-\alpha)(x_i^a - \overline{x^a}) + \alpha\left(x_i^f - \overline{x^f}\right),\ 0 \le \alpha \le 1 \quad (18)$$

where α was set to 0.975 in this study.

3. Synthetic experiments

3.1. Simple 2-D slope with homogeneous hydraulic conductivity

3.1.1. Experiment Design

The synthetic experiment was implemented to examine how topography-driven surface lateral flows contribute to efficiently propagating observation's information horizontally in the data assimilation of soil moisture observation. Two synthetic reference runs were created by Parflow. The 2-D domain has a horizontal extension of 4000m and a vertical extension of 5m. The domain of the virtual slope was horizontally discretized into 40 grid cells with a grid cell size of 100m and vertically discretized into 50 grid cells with a grid cell size of 0.10m. The domain has a 25% slope. In two synthetic reference runs, it heavily rains only in the upper half of the slope (2000m<x<4000m). A constant rainfall rate of 50mm/h was applied for 3 hours and then the period with no rainfall and evaporation of 0.075mm/h lasted for 117 hours. This 120-hour rain/no rain cycle was repeatedly applied to the domain. The configurations described above were schematically shown in Figure 1a. The parameters of the van Genuchten relationship, alpha and n, were set to 1.5 and 1.75, respectively. The porosity, ϕ in equation (1), was set to 0.40. The Manning's coefficient, n in equation (5), was set to 5.52×10^{-6} [$m^{-1/3}h$]. The initial groundwater table was located in z=3m and the hydrostatic pressure gradient was assumed for the initial pressure heads in the unsaturated soil layers.

The difference between two synthetic reference runs is the value of saturated hydraulic conductivity. The surface saturated hydraulic conductivity, $K_{s,surface}$ in equation (3), was set to 0.005 [m/h] in one reference, and 0.02 [m/h] in the other. Figure 1 shows the difference of the response to heavy rainfall between the two synthetic reference runs. In the case of the low saturated hydraulic conductivity (hereafter called the LOW_K reference), larger surface lateral flows are generated than the case of the high saturated hydraulic conductivity (hereafter called the HIGH_K reference). In the LOW_K reference, the topography-driven surface lateral flows reach the left edge of the domain (Figure 1b). In the HIGH_K reference, supplied water moves vertically rather than horizontally and the topography-driven surface flows reach around x = 1000~1500m (Figure 1d).

For the data assimilation experiment, an ensemble of 50 realizations were generated. Each ensemble member has different saturated hydraulic conductivity and rainfall rate. Lognormal multiplicative noise was added to surface saturated hydraulic conductivity and rainfall rate of the synthetic reference runs. The two parameters of the lognormal distribution, commonly called μ and σ, were set to 0 and 0.15, respectively. The initial groundwater depth of each ensemble member was drawn from the uniform distribution from 2.0m to 3.5m and the hydrostatic pressure gradient was assumed for the initial pressure heads in the unsaturated soil layers.

The virtual hourly observations were generated by adding the Gaussian white noise whose mean is zero to the volumetric soil moisture simulated by the synthetic reference runs. The observation error (the standard deviation of the added Gaussian white noise) was set to 0.05 m^3/m^3. It was assumed that the volumetric soil moistures can be observed in every soil layer from surface to the depth of 1m at the specific location. The two scenarios of the observation's location are provided. In the first scenario (hereafter called the UP_O scenario), the volumetric soil moisture at the upper part of the slope (x = 2500m) was observed. In the UP_O scenario, I could observe the volumetric soil moisture in the upper part of the slope where it heavily rains and tried to infer the soil moisture in the lower part of the slope where it does not rain by propagating the observation's information downhill. In the second scenario (hereafter called the DOWN_O scenario), the volumetric soil moisture at the lower part of the slope (x = 1500m) was observed. In the DOWN_O scenario, I could observe the volumetric soil moisture in the lower part of the slope where it does not rain and tried to infer the soil moisture in the upper part of the slope where it heavily rains by propagating the observation's information uphill.

Since I had the two synthetic reference runs (the HIGH_K and LOW_K references) and the two observation scenarios (the UP_O and DOWN_O scenarios), I implemented totally four data assimilation experiments. Table 1 summarizes the data assimilation experiments implemented in this study. For instance, in the HIGH_K-UP_O experiment, I chose the HIGH_K reference and generated an ensemble of 50 realizations from the HIGH_K reference. The soil moisture observations were generated from the HIGH_K reference at the location of x = 2500m and assimilated into the model every hour. The simulated volumetric soil moisture of the data assimilation experiment was compared with that of the HIGH_K reference.

In the data assimilation experiments, I adjusted pressure head by data assimilation so that x^f in section 2.2 is pressure head. Since the surface saturated hydraulic conductivity was also adjusted, x^f in section 2.2 includes $K_{s,surface}$. It should be noted that I adjusted a single surface saturated hydraulic conductivity which is applied to the whole domain so that the estimated parameter was not spatially distributed. Spatial regularization has been applied to calibrate spatially distributed parameters by adjusting a single parameter (Pokhrel and Gupta 2010). I suppose to apply the spatial regularization in the real-world application of the hyperresolution land data assimilation. Since I assimilated volumetric soil moisture observations (y^f and y^o in section 2.2 are simulated and observed volumetric soil moisture, respectively), the van Genuchten relationship works as an observation operator $\mathcal{H}$ in this study.

In addition to the data assimilation (DA) experiments, I implemented the NoDA experiment (also called the open-loop experiment in the literatures of the LDAS study) in which the ensemble was used but no observation data were assimilated. As evaluation metrics, root-mean-square-error (RMSE) was used:

$$\mathrm{RMSE} = \sqrt{\frac{1}{k}\sum_{i=1}^{k}(F_i - T)^2} \quad (19)$$

where k is the ensemble number, F_i is the volumetric soil moisture simulated by the i-th member in the DA or NoDA experiment, T is the volumetric soil moisture simulated by the synthetic reference run.

To evaluate the impact of data assimilation, the improvement rate (IR) was defined and calculated by the following equation:

$$\mathrm{IR} = \frac{\overline{RMSE_{DA}} - \overline{RMSE_{NoDA}}}{\overline{RMSE_{NoDA}}} \quad (20)$$

where $\overline{RMSE_{DA}}$ and $\overline{RMSE_{NoDA}}$ are time-mean RMSE of the DA and NoDA experiments, respectively. The negative IR indicates that data assimilation positively impacts the simulation of soil moisture.

Four of 120-hour rain/no rain cycles were applied so that the computation period was 480 hours. The spin-up results in the first 120 hours were not used to calculate the evaluation metrics.

3.1.2. Results

Figure 2a shows the IR of the LOW_K-UP_O experiment. The time series of the DA and NoDA experiment and the synthetic reference run in the LOW_K-UP_O experiment can be found in Figure S1. The data assimilation efficiently propagates the information of the observations located in the upper part of the slope (see the black arrow in Figure 2a) both horizontally and vertically. RMSE is reduced by data assimilation not only directly under the observation but also the lower part of the slope where it does not rain. The optimized $K_{s,surface} \approx 0.00508$ is also accurate. However, the increase of RMSE by data assimilation can be found at the left edge of the domain, which is far from the location of the observation. Please note that the impact of data assimilation on the surface soil moisture simulation is small because the RMSE of the NoDA experiment is already small ($\leq 0.01 m^3/m^3$) there in the case of the LOW_K reference.

Figure 2b shows the IR of the LOW_K-DOWN_O experiment (see also Figure S2 for time series). The IR's spatial pattern of the LOW_K-DOWN_O experiment is similar to that of the LOW_K-UP_O experiment. It is promising that I can accurately infer soil moisture in the region where it heavily rains from the shallow soil moisture observations in the region where it does not rain. The optimized $K_{s,surface} \approx 0.00512$ is also accurate.

Figure 3a shows the difference of time-mean RMSEs ($\overline{RMSE_{DA}}$ in equation (20)) between the LOW_K-UP_O and LOW_K-DOWN_O experiments. Although observing the lower part of the slope slightly improves the soil moisture simulation at the left edge of the domain compared with observing the upper part of the slope, there are few differences between the UP_O and DOWN_O scenarios in the case of the LOW_K reference. In the data assimilation system of this study, the soil moisture observations have large representativeness and I can efficiently infer soil moisture in the soil columns which are horizontally and vertically far from the observations.

Figure 2c shows the IR of the HIGH_K-UP_O experiment (see also Figure S3 for time series). The data assimilation significantly reduces RMSE of the soil moisture simulation directly under the observations (see the black arrow in Figure 2c), which indicates that the data assimilation efficiently propagates the information of the observations vertically. The saturated hydraulic conductivity is also accurately optimized ($K_{s,surface} \approx 0.0204$). However, the impact of the data assimilation on the soil moisture simulation in the lower part of the slope around x=1500m is marginal although there are large RMSE in the NoDA experiment (>0.05m^3/m^3) at the edge of the area where topography-driven surface flows reach in the HIGH_K reference (see Figure 1d).

Figure 2d shows the IR of the HIGH_K-DOWN_O experiment (see also Figure S4 for time series). Although the observations in the lower part of the slope (see the black arrow in Figure 2d) significantly improve the soil moisture simulation in the downstream area of the observation and accurately optimize $K_{s,surface} \approx 0.0208$, the impact of the data assimilation on the shallow soil moisture simulation around x=500~1000m is marginal. As I found in the LOW_K-DOWN_O experiment, the shallow soil moisture observations in the region where it does not rain can improve the soil moisture simulation in the region where it heavily rains. However, the IR of the HIGH_K-DOWN_O experiment in the upper part of the slope is smaller than that of the LOW_K-DOWN_O experiment (see Figure 2b and 2d).

The high representativeness of the observations which I found in the case of the LOW_K reference cannot be found in the case of the HIGH_K reference. Figure 3b shows the difference of time-mean RMSEs ($\overline{RMSE_{DA}}$ in equation (20)) between the HIGH_K-UP_O and HIGH_K-DOWN_O experiments. Compared with the LOW_K reference case (Figure 3a), there are significant differences between the UP_O and DOWN_O scenarios in the case of higher saturated hydraulic conductivity. In this case, the vertical propagation of the observations' information is more efficient than the horizontal propagation.

The relatively low efficiency of the data assimilation and the low representativeness of the soil moisture observations in the case of the HIGH_K reference are caused by the non-Gaussian background error distribution. To evaluate the non-Gaussianity of the background error sampled by an ensemble, I used the Kullback-Leibler divergence (KLD) (Kullback and Leibler 1951):

$$D_{KL}(p,q) = \sum_i p(i) log \frac{p(i)}{q(i)} \quad (21)$$

where $D_{KL}(p,q)$ is the KLD between two probabilistic distribution functions (PDFs), p and q. If two PDFs are equal for all i, $D_{KL}(p,q) = 0$. A large value for $D_{KL}(p,q)$

indicates that p and q are not close to each other. Therefore, the KLD is appropriate as a benchmark to evaluate the closeness of two PDFs. It should be noted that the KLD is not symmetric ($D_{KL}(p,q) \neq D_{KL}(q,p)$). In this study, I compared the PDF of the NoDA ensemble (p in equation (21)) with the Gaussian PDF which has the mean and variance of the NoDA ensemble (q in equation (21)).

Figure 4 shows that the NoDA ensemble in the case of the HIGH_K reference has stronger non-Gaussianity than the case of the LOW_K reference especially in the shallow soil layers. The strong non-Gaussianity of the NoDA ensemble generated from the HIGH_K reference can be found at the edge of the area where topography-driven surface flows reach (Figure 1d). Figure 5 shows that there is the bifurcation of the ensemble in this region when the ensemble is generated from the HIGH_K reference. The process of topography-driven surface flows is switched on if and only if the surface soil is saturated (see equation (4)) so that the ensemble tends to be bifurcated into the members with surface flows and without surface flows. As I mentioned in section 2.2, in the ETKF, the state and parameter variables are adjusted assuming the Gaussian PDF of the model's error and the linear relationship between observed variables and unobserved variables. Therefore, the non-Gaussianity of the prior ensemble induced by the strong non-linear dynamics of surface lateral flows makes the ETKF inefficient. It should be noted that the non-Gaussianity can also be found in the LOW_K reference at the edge of the domain (x=500m) due to the non-linear dynamics, which causes the degradation of the soil moisture simulation in the LOW_K-UP_O experiment (see Figure 2a).

It should be noted that the improvement of the soil moisture simulation cannot be found if the topography-driven surface flows are neglected. Figure S5 shows the IR of the LOW-K_DOWN-O experiment where the topography-driven surface flows are neglected in the ParFlow simulation. The imperfect model physics of ParFlow substantially degrades the skill to simulate soil moisture and data assimilation cannot compensate this degradation. This point will also be discussed in the section 3.2 more deeply.

3.2. Simple 3-D slope with heterogeneous hydraulic conductivity

3.2.1. Experiment design

To further demonstrate how land data assimilation works with topography-driven surface lateral flows, I implemented another synthetic experiment which is more realistic than that shown in section 3.1. The 3-D domain has a horizontal extension of 4000 m×4000m and a vertical extension of 3m. The domain was horizontally discretized into 40×40 grid cells with a grid cell size of 100m×100m and vertically discretized into 30 grid cells with a grid cell size of 0.1m. The domain has a 10% slope in both x and y directions (see Figure 6a). The parameters of the van Genuchten relationship, porocity and Manning's coefficient were set to the same variables as the synthetic experiment in section 3.1.

The spatially heterogeneous surface saturated hydraulic conductivity was generated following Kurtz et al. (2016). The field of $log_{10}(K_{s,surface})$ was generated by two dimensional unconditioned sequential Gaussian simulation. A Gaussian variogram whose nugget, sill, and range are 0.0 $log_{10}(\mathrm{m/h})$, 0.1 $log_{10}(m^2h^2)$, and 12 model grids (1200m) was used to simulate the spatial distribution of $log_{10}(K_{s,surface})$. A constant value of -2.30 $log_{10}(\mathrm{m/h})$ (i.e. 0.005 (m/h)) was added to the generated field. Subsurface saturated hydraulic conductivity was calculated by equation (3). An ensemble of 51 realizations of $log_{10}(K_{s,surface})$ was generated and one of them was chosen as a synthetic reference (Figure 6a). The remaining 50 members were used for data assimilation experiments.

A rainfall rate $\mathrm{R(x,y)}$ (mm/h) was modelled by a logistic function:

$$\mathrm{R(x,y)} = \frac{R_{max}}{1 + 100\mathrm{exp}(-0.2 \times \frac{x+y}{2})}$$

where x and y are horizontal grid numbers ($1 \leq \mathrm{x} \leq 40, 1 \leq \mathrm{y} \leq 40$). In the synthetic reference, the maximum rainfall rate in the domain, R_{max}, was set to 50 (mm/h) (Figure 6b). This rainfall rate was applied for 3 hours and then the period with no rainfall and evaporation of 0.075mm/h lasted for 117 hours. For data assimilation experiment, an ensemble of 50 realization of $\mathrm{R(x,y)}$ was generated by adding a lognormal multiplicative noise to R_{max} of the synthetic reference. The two parameters of the lognormal distribution, commonly called μ and σ, were set to 0 and 0.15, respectively.

Figure 6c shows the distribution of surface soil moisture in the synthetic reference run. Strong rainfall rate applied in the upper part of the slope generates the topography-driven surface lateral flows. The virtual hourly observations were generated by adding the Gaussian white noise, whose mean is zero and standard deviation is 0.05 m^3/m^3, to the volumetric surface soil moisture simulated by the synthetic reference run. Unlike the experiment in section 3.1, only surface soil moisture can be observed in this synthetic experiment, which makes this experiment more realistic. Three different observing networks with different observation densities were used (Figure 7). The observing networks shown in Figure 7a, 7b, and 7c have totally 1, 9, and 361 observations and are called obs1, obs9, and obs361, respectively.

In the DA experiments, those virtual observations of surface soil moisture were assimilated every hour to adjust pressure head and saturated hydraulic conductivity. As I did in the section 3.1, the NoDA experiments were also implemented. The two different configurations of ParFlow were used for both DA and NoDA experiments. In the first configuration, called OF, Parflow explicitly solves overland flows. In the second configuration, called noOF, Parflow assumes the flat terrain for surface flows so that no overland flows are generated. Since the synthetic reference run explicitly considers the topography-driven surface flows, the configuration of noOF assumes that the model physics is imperfect. I implemented 8 numerical experiments which are summarized in Table 2. For example, the OF_DA_obs9 experiment is the data assimilation experiment with the observing network shown in Figure 7b, in which Parflow explicitly solves topography-driven surface flows. The noOF_NoDA is the model run without assimilating observations, in which Parflow does not consider topography-driven surface flows.

3.2.2. Results

Figure 8a shows the RMSE of soil moisture simulation of a second soil layer in all 8 experiments. When Parflow explicitly solves topography-driven surface flows, data assimilation substantially reduces RMSE of the soil moisture simulation (green bars in Figure 8a). The OF_DA_obs361 experiment has the smallest RMSE so that a denser observing network is beneficial to estimate soil moisture. Figure 8b shows the RMSE of the estimation of saturated surface hydraulic conductivity in all 8 experiments. Data assimilation also reduces the uncertainty in model's parameters (green bars in Figure 8b). However, the OF_DA_obs361 experiment has larger RMSE than the other DA experiments. This is because the adjustment of hydraulic conductivity in the OF_DA_obs361 experiment is overfitting to observations. In the OF configuration, there are two sources of errors, rainfall rate and hydraulic conductivity. However, data assimilation can adjust only hydraulic conductivity so that the assimilation of a large number of observations causes overfitting to mitigate the impact of errors in rainfall rate.

The noOF_NoDA experiment has larger RMSE than the OF_NoDA experiment due to the neglect of topography-driven surface flows. In the noOF configuration, data assimilation also substantially improves the soil moisture simulation (red bars in Figure 8a). The noOF_DA_obs361 experiment outperforms the OF_NoDA experiment so that data assimilation with a dense observing network can compensate the negative impact of neglecting topography-driven surface flows. Although data assimilation positively impacts the parameter estimation, the denser observing network cannot reduce RMSE of hydraulic conductivity estimation (red bars in Figure 8b). The negative impact of the dense observations in the noOF_DA_obs361 experiment on the parameter estimation is larger than the OF_DA_obs361 experiment. In addition to rainfall rate and hydraulic conductivity, the imperfect model physics (i.e., no topography-driven surface flows) is the source of error in the noOF configuration. The assimilation of a large number of observations causes overfitting because it mitigates the impact of all systematic errors which comes from three different sources only by adjusting hydraulic conductivity.

Figure 9 shows the difference of RMSE of the soil moisture simulation between the DA experiments and the OF_NoDA experiment. In the DA configuration, the improvement of the soil moisture estimation can be found in the large area even if there is a single observation in the center of the domain (Figure 9a). Figure 9b shows that the increase of the number of observations substantially improves the soil moisture simulation in the region where the topography-driven surface flows reach (see also Figure 6c). However, the skill to simulate soil moisture is severely degraded in the lower-left corner of the domain, which causes the stalled improvement from the OF_DA_obs1 experiment to the OF_DA_obs9 experiment shown in Figure 8a. Figure 9c shows that although the far denser observing network can slightly mitigate this degradation, increasing the number of observations cannot efficiently solve this issue. This degradation is caused by the bifurcation of ensemble members at the edge of the area where topography-driven surface flows reach (Figure S6). Figure 10 shows KLD in the OF_NoDA and noOF_NoDA_experiments. Figure 10a clearly shows that the ensemble simulation generates the strong non-Gaussianity at the edge of the area where topography-driven surface flows reach, which harms the efficiency of the ETKF. This finding is consistent to what I found in the previous experiment in section 3.1.

In the noOF configuration, there are large errors in the area around 500<=x, y <=1500 since the increase of soil moisture in this area is caused by topography-driven surface flows which is neglected in the noOF configuration. Figures 9d and 9e show that the sparse observations cannot completely remove this degradation caused by imperfect model physics. Figure 9f shows that the noOF_DA_obs361 can outperform the

OF_NoDA experiment in exchange for the degradation of the parameter estimation as I found in Figure 8. The unstable behavior of the ETKF found in the OF configuration does not occur when the topography-driven surface flows are neglected since the ensemble simulation does not generate the non-Gaussian prior distribution (Figure 10b).

4. Discussion

In this study, I revealed that the hyperresolution integrated surface-subsurface hydrological model gives the unique opportunity to effectively use soil moisture observations to improve the soil moisture simulation. I found that the explicit calculation of topography-driven surface flows has an important role in propagating the information of soil moisture observation horizontally by data assimilation even if there is considerable heterogeneity of meteorological forcing. It is possible that the soil moisture observations in the area where it does not heavily rain can improve the soil moisture simulation in the severe rainfall area. This new potential of hyperresolution land data assimilation is expected to be useful to monitor and predict flash floods induced by local severe rainfall on complex terrain.

This potential cannot be brought out in the conventional 1-D LSM where sub-grid scale surface runoff is parameterized and the surface flows in one grid do not move to the adjacent grids. Neglecting topography-driven surface flows causes significant bias in the soil moisture simulation and this bias cannot be completely mitigated by data assimilation especially in the case of a sparse observing network. However, I found that assimilating soil moisture observations into the model's three dimensional state and parameter space can stably improve the skill to estimate soil moisture and hydraulic conductivity even if the model has the imperfect physics which cannot simulate the generation of strong surface runoff. This finding implies that the conventional 1-D LSM with full 3-D data assimilation may be a computationally cheap and reasonable choice in some cases.

The conventional ensemble data assimilation (i.e. ETKF) severely suffers from the non-Gaussian background error PDFs caused by the strongly nonlinear dynamics of topography-driven surface flows. The efficiency of ETKF to propagate the information of observations horizontally in the model space is limited in the edge of the area where topography-driven surface flows reach. It should be noted that the low representativeness of the soil moisture observations in the case of the HIGH_K reference shown in section 3.1 is due to the core assumption of the Kalman filter that the error PDFs follow the

Gaussian distribution so that the increase of the ensemble size cannot solve this issue. I implemented the data assimilation experiment in the case of the HIGH_K reference with the 500 ensemble size, which is 10 times larger than the experiments shown in section 3.1, and found no significant improvement of the soil moisture simulation (not shown).

The results of the HIGH_K-UP_O and the HIGH_K-DOWN_O imply that the spatially dense soil moisture observations are needed to efficiently constrain state variables at the edge of surface flows. High resolution soil moisture remote sensing based on satellite active and passive combined microwave observations (e.g., He et al. 2018) and the assimilation of those data (Lievens et al. 2017) may be the important technologies in the era of the hyperresolution land modeling. The high resolution observations of surface inundated water from satellite imagery (e.g., Sakamoto et al. 2007 RSE; Arnesen et al. 2013 RSE) may also be useful. However, the more realistic numerical experiment in section 3.2 implies that the dense observing network of surface soil moisture cannot completely remove the negative impact of the non-Gaussian background PDF.

Since there is the nonlinear relationship between observed and unobserved variables sampled by an ensemble, a localization method, which spatially restricts the impact of assimilating observation, is crucially needed for the real-world application. The results of this study imply that the optimal localization radius strongly depends on the model parameter (i.e. saturated hydraulic conductivity). Rasmussen et al. (2015) successfully applied the adaptive localization method (Anderson 2007; Bishop and Hodyss 2009) to the data assimilation of groundwater observations into a hydrological model. It is appropriate to adaptively determine the localization radius considering the lack of prior knowledge of how soil moistures simulated by an ensemble are horizontally correlated.

Reducing the uncertainty in rainfall positively impacts the efficiency of data assimilation since the bifurcation of simulated soil moisture found in Figure 5c is originally induced by the uncertainty in rainfall. Although assimilating land hydrological observations to improve the rainfall input has been intensively investigated (e.g., Sawada et al. 2018; Herrnegger et al. 2015; Crow et al. 2011; Vrugt et al. 2008), it has yet to be applied to the hyperresolution land models. It should be noted that the parameters of the lognormal distribution to model the uncertainty in rainfall were specified to make the rainfall PDF similar to the Gaussian distribution. I chose the lognormal distribution in order not to generate the negative value of rainfall and I did not intend to introduce non-Gaussianity into the external forcing. The rainfall input which follows the Gaussian PDF was transformed into the non-Gaussian PDF of the background error by the strongly nonlinear dynamics of topography-driven surface flows.

To explicitly consider the non-Gaussianity and non-linear relationship between observed and unobserved variables induced by topography-driven surface flows, the particle filters may be useful. The particle filtering can represent a probability distribution (including non-Gaussian distributions) directly by an ensemble. The particle filters have been intensively applied to conventional 1-D LSMs (e.g., Sawada et al. 2015; Qin et al. 2009) and lumped hydrological models (e.g., Yan and Moradkhani 2016; Vrugt et al. 2013). Although particle filtering in the high dimensional system suffers from the "curse of dimensionality" (e.g., Snyder et al. 2008), the applicability of particle filtering to the 3-D hyperresolution land models should be assessed in the future.

Since the synthetic numerical experiment implemented in this paper assumed the extreme heterogeneity of rainfall, the findings of this paper may be exaggerated. In the future work, the contributions of the topography-driven surface runoff process to the data assimilation of hydrological observations should be quantified in the real-world application. In addition, in the virtual experiment of this paper, I neglected some of the important land processes such as transpiration, canopy interception, snow, and frozen soil. Although they are generally not important processes in terms of the generation of topography-driven surface lateral flows, those processes should be considered in the future.

5. Conclusions

Lateral surface flows induced by heavy rainfalls do matter for data assimilation of soil moisture observations into hyperresolution land models. Even if there is extreme heterogeneity of rainfall, I can effectively propagate the information of the soil moisture observations horizontally in the model space and improve the soil moisture simulation by the ensemble Kalman filter. This new capability of the data assimilation with the hyperresolution land models may innovate the monitor and prediction of flash floods caused by local severe rainfalls. However, the non-Gaussianity of the model error induced by the nonlinear dynamics of topography-driven surface flows harms the efficiency of the data assimilation of soil moisture observations. It is difficult to efficiently constrain model states at the edge of the area where topography-driven surface flows reach by linear-Gaussian filters, which brings the new challenge in land data assimilation for hyperresolution land models.

Acknowledgement

All data used in this paper are stored in the repository of Meteorological Research Institute for 5 years and available upon request to Y. Sawada. The ETKF code used in this study is based on the open source available at https://github.com/takemasa-miyoshi/letkf. This study was supported by the JSPS KAKENHI grant JP17K18352.

References

Ait-El-Fquih, B., El Gharamti, M., & Hoteit, I. (2016). A Bayesian consistent dual ensemble Kalman filter for state-parameter estimation in subsurface hydrology. *Hydrology and Earth System Sciences*, *20*(8), 3289–3307. https://doi.org/10.5194/hess-20-3289-2016

Amesen et al. (2013). Monitoring flood extent in the lower Amazon River floodplain using ALOS/PALSAR ScanSAR images. *Remote Sensing of Environment, 130*, 51-61. https://doi.org/10.1016/j.rse.2012.10.035

Anderson, J. L. (2007). Exploring the need for localization in ensemble data assimilation using a hierarchical ensemble filter. *Physica D: Nonlinear Phenomena*, *230*(1–2), 99–111. https://doi.org/10.1016/j.physd.2006.02.011

Bandara, R., Walker, J. P., & Rüdiger, C. (2014). Towards soil property retrieval from space: Proof of concept using in situ observations. *Journal of Hydrology, 5*12, 27–38. https://doi.org/10.1016/j.jhydrol.2014.02.031

Bandara, R., Walker, J. P., Rüdiger, C., & O. Merlin (2015). Towards soil property retrieval from space: An application with disaggregated satellite observations. *Journal of Hydrology, 522,* 582-593, https://doi.org/10.1016/j.jhydrol.2015.01.018

Beven, K. (1982), On subsurface stormflow: an analysis of response times, *Hydrological Science Journal*, *27,* 505-521, doi:10.1080/02626668209491129

Bishop, C.H., Etherton, B., J., & Majumdar, S., J., (2001). Adaptive Sampling with the Ensemble Transform Kalman Filter. Part I: Theoretical Aspects. *Monthly. Weather. Review.*, ***129***, 420–436, https://doi.org/10.1175/1520-0493(2001)129<0420:ASWTET>2.0.CO;2

Bishop, C. H., & Hodyss, D., (2009) Ensemble covariances adaptively localized with ECO-RAP. Part 1: Tests on simple error models. *Tellus, 61A*, 84–96.

Camporese, M., Paniconi, C., Putti, M., & Salandin, P. (2009). Ensemble Kalman filter data assimilation for a process-based catchment scale model of surface and subsurface flow. *Water Resources Research*, *45*(10), 1–14. https://doi.org/10.1029/2008WR007031

Camporese, M., Paniconi, C., Putti, M., & Orlandini, S. (2010). Surface-subsurface flow modeling with path-based runoff routing, boundary condition-based coupling, and assimilation of multisource observation data. *Water Resources Research*, *46*(2). https://doi.org/10.1029/2008WR007536

Crow, W. T., Van Den Berg, M. J., Huffman, G. J., & Pellarin, T. (2011). Correcting rainfall using satellite-based surface soil moisture retrievals: The Soil Moisture Analysis Rainfall Tool (SMART). *Water Resources Research*, *47*(8), 1–15. https://doi.org/10.1029/2011WR010576

Fang, Y., L. R. Leung, Z. Duan, M. S. Wigmosta, R. M. Maxwell, J. Q. Chambers, & J. Tomasella (2017), Influence of landscape heterogeneity on water available to tropical forests in an Amazonian catchment and implications for modeling drought response, *J. Geophys. Res. Atmos.*, *122*, doi:10.1002/2017JD027066.

Han, X., Franssen, H.-J. H., Montzka, C. & Vereecken, H. (2014). Soil moisture and soil properties estimation in the Community Land Model with synthetic brightness temperature observations, *Water Resources Research., 50,* 6081 – 6105, doi:10.1002/2013WR014586.

Herrnegger, M., Nachtnebel, H. P., & Schulz, K. (2015). From runoff to rainfall : inverse rainfall – runoff modelling in a high temporal resolution, 4619–4639. https://doi.org/10.5194/hess-19-4619-2015

He, L., Hong, Y., Wu, X., Ye, N., Walker, J. P. & Chen, X. (2018). Investigation of SMAP Active–Passive Downscaling Algorithms Using Combined Sentinel-1 SAR and SMAP Radiometer Data. *IEEE Transactions on Geosciences and Remote Sensing*, *56*, 4906-4918, doi: 10.1109/TGRS.2018.2842153.

Hendricks Franssen, H. J., & Kinzelbach, W. (2008). Real-time groundwater flow modeling with the Ensemble Kalman Filter: Joint estimation of states and parameters and the filter inbreeding problem. *Water Resources Research*, *44*(9), 1–21. https://doi.org/10.1029/2007WR006505

Houborg, R., Rodell, M., Li, B., Reichle, R., & Zaitchik, B. F. (2012). Drought indicators based on model-assimilated Gravity Recovery and Climate Experiment (GRACE) terrestrial water storage observations. *Water Resources Research*, *48*(7). https://doi.org/10.1029/2011WR011291

Houtekamer, P. L., & Zhang, F. (2016). Review of the Ensemble Kalman Filter for Atmospheric Data Assimilation. *Monthly Weather Review*, MWR-D-15-0440.1. https://doi.org/10.1175/MWR-D-15-0440.1

Hunt, B. R., Kostelich, E. J., & Szunyogh, I. (2007). Efficient data assimilation for spatiotemporal chaos: A local ensemble transform Kalman filter. *Physica D: Nonlinear Phenomena*, *230*(1–2), 112–126. https://doi.org/10.1016/j.physd.2006.11.008

Ji, P., Yuan, X., & Liang, X. Z. (2017). Do Lateral Flows Matter for the Hyperresolution Land Surface Modeling? *Journal of Geophysical Research: Atmospheres*, 1–16. https://doi.org/10.1002/2017JD027366

Keune, J., F. Gasper, K. Goergen, A. Hense, P. Shrestha, M. Sulis, & S. Kollet (2016), Studying the influence of groundwater representations on land surface-atmosphere feedbacks during the European heat wave in 2003, *Journal of Geophysical Research. Atmospheres*, 121, 13,301–13,325, doi:10.1002/2016JD025426.

Kollet, S. J., & Maxwell, R. M. (2006). Integrated surface–groundwater flow modeling: A free-surface overland flow boundary condition in a parallel groundwater flow model. *Advances in Water Resources*, *29*(7), 945–958. https://doi.org/10.1016/j.advwatres.2005.08.006

Kumar, S. V., Reichle, R. H., Koster, R. D., Crow, W. T., & Peters-Lidard, C. D. (2009). Role of Subsurface Physics in the Assimilation of Surface Soil Moisture Observations.

Journal of Hydrometeorology, *10*(6), 1534–1547. https://doi.org/10.1175/2009JHM1134.1

Kurtz, W., He, G., Kollet, S. J., Maxwell, R. M., Vereecken, H., & Franssen, H. J. H. (2016). TerrSysMP-PDAF (version 1.0): A modular high-performance data assimilation framework for an integrated land surface-subsurface model. *Geoscientific Model Development*, *9*(4), 1341–1360. https://doi.org/10.5194/gmd-9-1341-2016

Kullback, S., & Leibler, R. A. (1951). On information and sufficiency, *The Annals of Mathematical Statistics*, *22*, 79-86

Lawrence, D. M., et al. (2011). Parameterization improvements and functional and structural advances in Version 4 of the Community Land Model. *Journal of Advances in Modeling Earth Systems*, *3*(3), 1–27. https://doi.org/10.1029/2011MS000045

Li, B., Rodell, M., Zaitchik, B. F., Reichle, R. H., Koster, R. D., & van Dam, T. M. (2012). Assimilation of GRACE terrestrial water storage into a land surface model: Evaluation and potential value for drought monitoring in western and central Europe. *Journal of Hydrology*, *446–447*, 103–115. https://doi.org/10.1016/j.jhydrol.2012.04.035

Lievens, et al. (2017). Joint Sentinel-1 and SMAP data assimilation to improve soil moisture estimates. *Geophysical Research Letters*, *44*(12), 6145–6153. https://doi.org/10.1002/2017GL073904

Martens, B., Miralles, D. G., Lievens, H., Schalie, R. Van Der, & Jeu, R. A. M. De. (2017). GLEAM v3 : satellite-based land evaporation and root-zone soil moisture, *Geoscientific Model Development*, *10*, 1903–1925. https://doi.org/10.5194/gmd-10-1903-2017

Maxwell, R. M., & N. L. Miller (2005). Development of a Coupled Land Surface and Groundwater Model. *Journal of Hydrometeorology*, *6*, 233-247. https://doi.org/10.1175/JHM422.1

Maxwell, R. M., & Condon, L. E. (2016). Connections between groundwater flow and transpiration partitioning. *Science*, *353*, 377-380, doi: 10.1126/science.aaf7891.

Maxwell, R. M., Condon, L. E., & Kollet, S. J. (2015). A high-resolution simulation of groundwater and surface water over most of the continental US with the integrated hydrologic model ParFlow v3, 923–937. https://doi.org/10.5194/gmd-8-923-2015

Maxwell, R. M., & Kollet, S. J. (2008). Interdependence of groundwater dynamics and land-energy feedbacks under climate change, *Nature Geoscience, 1,* 665–669. https://doi.org/10.1038/ngeo315

Maxwell, R. M., Lundquist, J. K., Mirocha, J. D., Smith, S. G., Woodward, C. S., & Tompson, A. F. B. (2011). Development of a Coupled Groundwater–Atmosphere Model. *Monthly Weather Review*, *139*(1), 96–116. https://doi.org/10.1175/2010MWR3392.1

Nerger, L., & Hiller, W., (2013). Software for ensemble-based data assimilation systems – implementation strategies and scalability. *Computers & Geosciences*. *55*, 110–118. http://dx. doi.org/10.1016/j.cageo.2012.03.026

Niu, G. Y., Paniconi, C., Troch, P. a., Scott, R. L., Durcik, M., Zeng, X., & Goodrich, D. C. (2014). An integrated modelling framework of catchment-scale ecohydrological processes: 1. Model description and tests over an energy-limited watershed. *Ecohydrology*, *7*(2), 427–439. https://doi.org/10.1002/eco.1362

Pokhrel, P., & Gupta, H. V. (2010). On the use of spatial regularization strategies to improve calibration of distributed watershed models. *Water Resources Research*, *46*(1), 1–17. https://doi.org/10.1029/2009WR008066

Qin, J., Liang, S., Yang, K., Kaihotsu, I., Liu, R., & Koike, T. (2009). Simultaneous estimation of both soil moisture and model parameters using particle filtering method through the assimilation of microwave signal. *Journal of Geophysical Research*, *114*(D15), 1–13. https://doi.org/10.1029/2008JD011358

Rasmussen, J., Madsen, H., Jensen, K. H., & Refsgaard, J. C. (2015). Data assimilation in integrated hydrological modeling using ensemble Kalman filtering: evaluating the effect of ensemble size and localization on filter performance. *Hydrology and Earth System Sciences*, *19*(7), 2999–3013. https://doi.org/10.5194/hess-19-2999-2015

Sakamoto, T., et al. (2007). Detecting temporal changes in the extent of annual flooding within the Cambodia and the Vietnamese Mekong Delta from MODIS time-series imagery. *Remote Sensing of Environement, 109,* 295-313. https://doi.org/10.1016/j.rse.2007.01.011.

Sawada, Y. & Koike, T. (2014). Simultaneous estimation of both hydrological and ecological parameters in an eco-hydrological model by assimilating microwave signal, *Journal of Geophysical Research – Atmospheres, 119,* 8839-8857, https://doi.org/10.1002/2014JD021536

Sawada, Y., Koike, T., & Walker, J. P. (2015). A land data assimilation system for simultaneous simulation of soil moisture and vegetation dynamics, *Journal of Geophysical Research – Atmospheres, 120,* 5910-5930, https://doi.org/10.1002/2014JD022895

Sawada, Y., Nakaegawa, T, & Miyoshi, T. (2018) Hydrometeorology as an inversion problem: Can river discharge observations improve the atmosphere by ensemble data assimilation?, *Journal of Geophysical Research - Atmospheres*, *123*, 848-860, https://doi.org/10.1002/2017JD027531

Sellers, P. J., et al. (1996). A revised land surface parameterization (SiB2) for atmospheric GCMs. Part I: Model formulation. *Journal of Climate.* https://doi.org/10.1175/1520-0442(1996)009<0676:ARLSPF>2.0.CO;2

Shrestha, P., Sulis, M., Masbou, M., Kollet, S., & Simmer, C. (2014). A Scale-Consistent Terrestrial Systems Modeling Platform Based on COSMO, CLM, and ParFlow. *Monthly Weather Review*, *142*(9), 3466–3483. https://doi.org/10.1175/MWR-D-14-00029.1

Snyder, C., Bengtsson, T., Bickel, P., & Anderson, J. (2008). Obstacles to High-Dimensional Particle Filtering. *Monthly Weather Review*, *136*(12), 4629–4640. https://doi.org/10.1175/2008MWR2529.1

Tian, W., Li, X., Cheng, G. D., Wang, X. S., & Hu, B. X. (2012). Coupling a groundwater model with a land surface model to improve water and energy cycle simulation. *Hydrology and Earth System Sciences*, *16*(12), 4707–4723. https://doi.org/10.5194/hess-16-4707-2012

Van Genuchten, M. T. (1980), A closed-form equation for predicting the hydraulic conductivity of unsaturated soils, *Soil Science Society of America Journal*, *44*, 892–898.

Verbeeck, H., Peylin, P., Bacour, C., Bonal, D., Steppe, K., & Ciais, P. (2011). fluxes in Amazon forests: Fusion of eddy covariance data and the ORCHIDEE model. Journal of Geophysical Research, 116(G2), 1–19. https://doi.org/10.1029/2010JG001544

Vrugt, J. A., ter Braak, C. J. F., Clark, M. P., Hyman, J. M., & Robinson, B. A. (2008). Treatment of input uncertainty in hydrologic modeling: Doing hydrology backward with Markov chain Monte Carlo simulation. *Water Resources Research*, *44*, 1–15. https://doi.org/10.1029/2007WR006720

Vrugt, J. A., ter Braak, C. J. F., Diks, C. G. H., & Schoups, G. (2013). Hydrologic data assimilation using particle Markov chain Monte Carlo simulation: Theory, concepts and applications. *Advances in Water Resources*, *51*, 457–478. https://doi.org/10.1016/j.advwatres.2012.04.002

Williams, J. L., & Maxwell, R. M. (2011). Propagating Subsurface Uncertainty to the Atmosphere Using Fully Coupled Stochastic Simulations. *Journal of Hydrometeorology*, *12*(4), 690–701. https://doi.org/10.1175/2011JHM1363.1

Wood, E. F., et al. (2011). Hyperresolution global land surface modeling : Meeting a grand challenge for monitoring Earth's terrestrial water, *Water Resources Research*, *47*, https://doi.org/10.1029/2010WR010090

Yan, H., & Moradkhani, H. (2016). Combined assimilation of streamflow and satellite soil moisture with the particle filter and geostatistical modeling. *Advances in Water Resources*, *94*, 364–378. https://doi.org/10.1016/j.advwatres.2016.06.002

Yang, K., Koike, T., Kaihotsu, I., & Qin, J. (2009). Validation of a Dual-Pass Microwave Land Data Assimilation System for Estimating Surface Soil Moisture in Semiarid Regions. *Journal of Hydrometeorology*, *10*(3), 780–793. https://doi.org/10.1175/2008JHM1065.1

Yang, K., Watanabe, T., Koike, T., Li, X., Fujii, H., Tamagawa, K., & Ishikawa, H. (2007). Auto-calibration System Developed to Assimilate AMSR-E Data into a Land Surface

Model for Estimating Soil Moisture and the Surface Energy Budget. *Journal of the Meteorological Society of Japan*, *85A*, 229–242. https://doi.org/10.2151/jmsj.85A.229

Zhang, F., Snyder, C., & Sun, J. (2004). Impacts of Initial Estimate and Observation Availability on Convective-Scale Data Assimilation with an Ensemble Kalman Filter. *Monthly. Weather. Review.*, **132**, 1238–1253, https://doi.org/10.1175/1520-0493(2004)132<1238:IOIEAO>2.0.CO;2

Zhang, H., Kurtz, W., Kollet, S., Vereecken, H., & Franssen, H. J. H. (2018). Comparison of different assimilation methodologies of groundwater levels to improve predictions of root zone soil moisture with an integrated terrestrial system model. *Advances in Water Resources*, *111*(May 2017), 224–238. https://doi.org/10.1016/j.advwatres.2017.11.003

Table 1. Configuration of the data assimilation experiments in section 3.1.

	hydraulic conductivity [m/h]	observation's location [m]
LOW_K-UP_O	0.005	2500
LOW_K-DOWN_O	0.005	1500
HIGH_K-UP_O	0.02	2500
HIGH_K-DOWN_O	0.02	1500

Table 2. Configuration of the data assimilation experiments in section 3.2

	overland flows	observing network
noOF_NoDA	none	no data assimilation
noOF_DA_obs1	none	Figure 7a
noOF_DA_obs9	none	Figure 7b
noOF_DA_obs361	none	Figure 7c
OF_NoDA	simulated	no data assimilation
OF_DA_obs1	simulated	Figure 7a
OF_DA_obs9	simulated	Figure 7b
OF_DA_obs361	simulated	Figure 7c

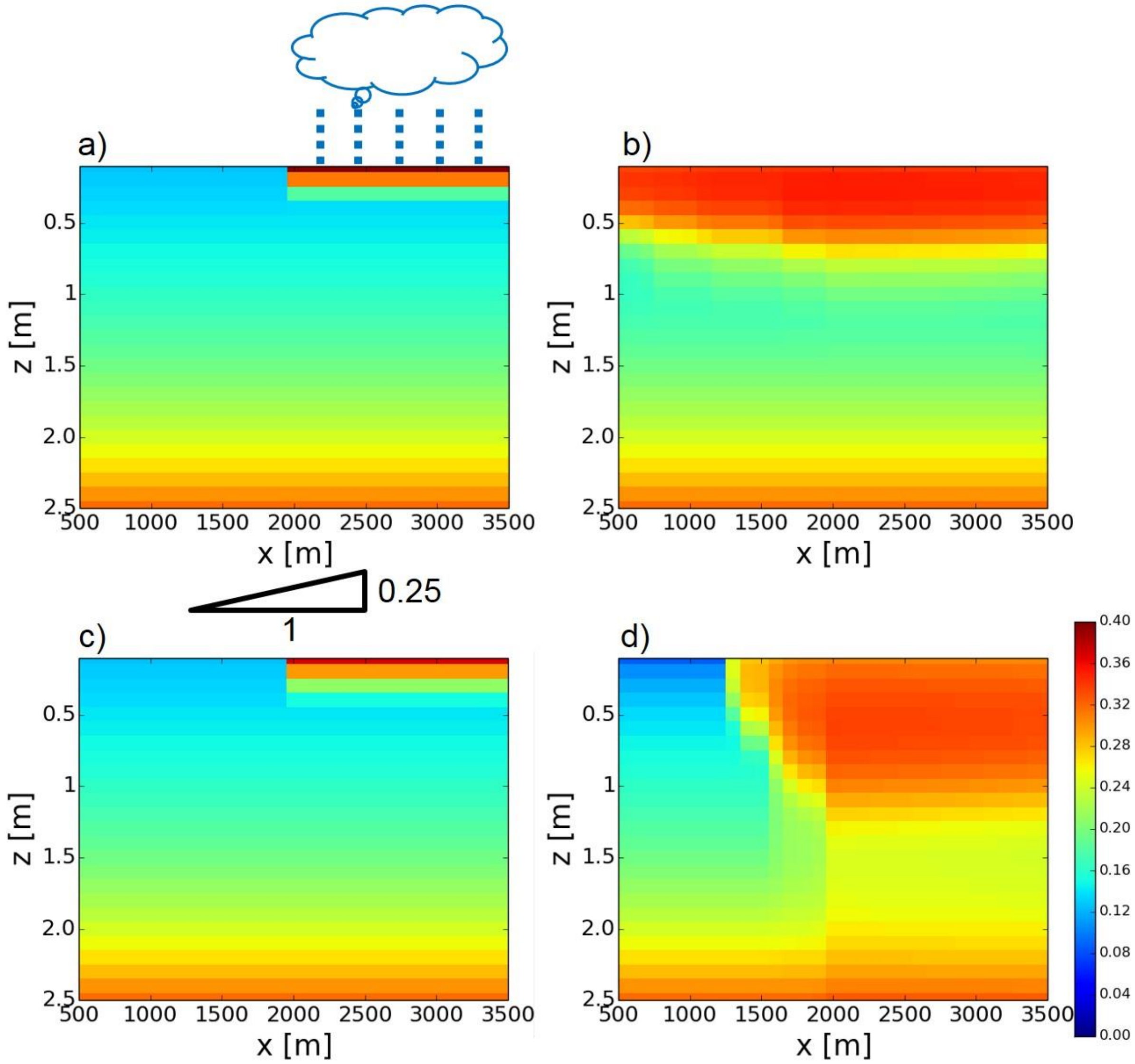

Figure 1. Distributions of volumetric soil moisture simulated by the synthetic reference runs. (a) The distribution of volumetric soil moisture [m^3/m^3] simulated by the LOW_K synthetic reference run at t = 0h. The schematic of the configuration of the synthetic reference runs is also shown (see also section 3). (b) same as (a) but at t = 130h. (c,d) same as (a,c) but for the HIGH_K synthetic reference run.

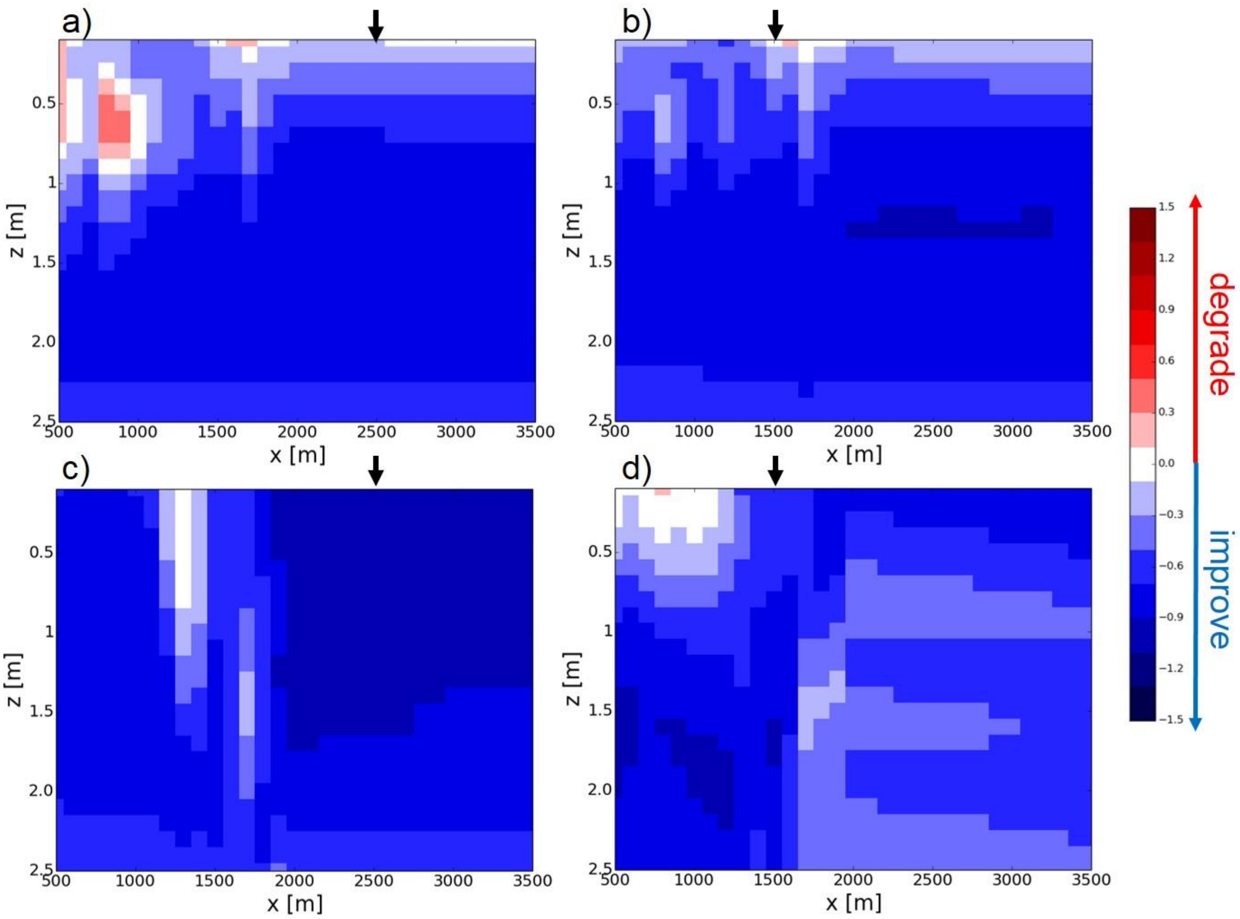

Figure 2. The improvement rates of the (a) LOW_K-UP_O, (b) LOW_K-DOWN_O, (c) HIGH_K_UP_O, (d) HIGH_K-DOWN_O experiments (see Table 1 and section 3). Black arrows show the locations of the soil moisture observations in each experiment.

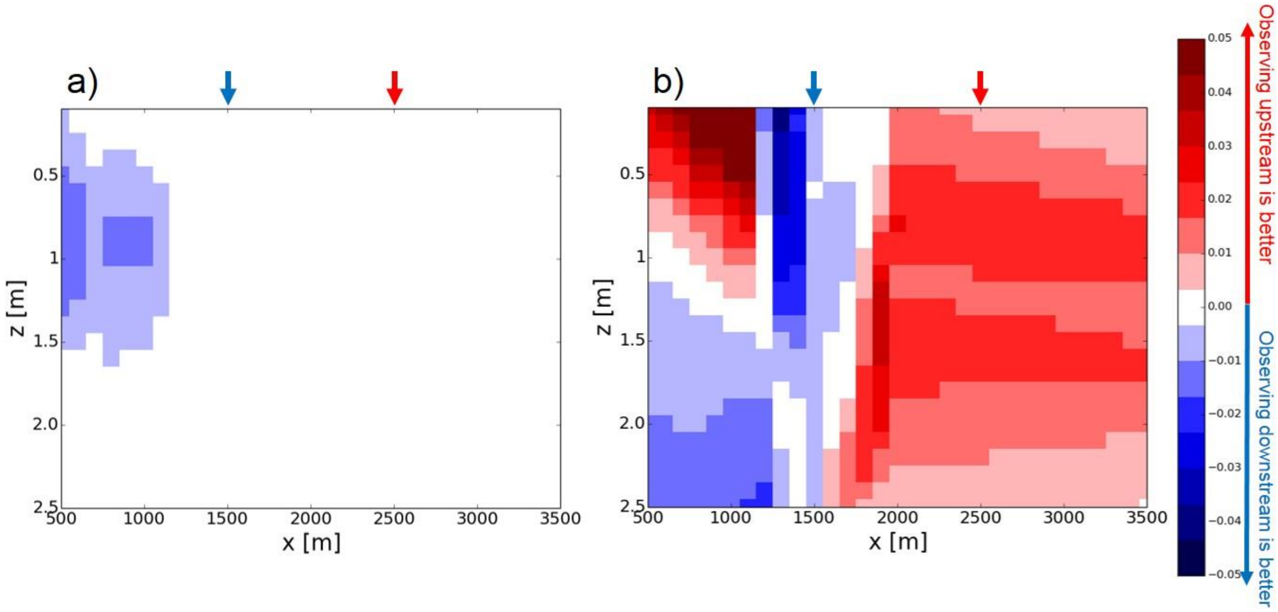

Figure 3. (a) The difference of time-mean RMSEs between the LOW_K-UP_O and LOW_K-DOWN_O experiments (see Table 1 and section 3). Red (blue) color indicates that the observations in the upper (lower) part of the slope reduce time-mean RMSE by data assimilation better than those in the lower (upper) part of the slope (see also arrows which are the locations of the observations). (b) same as (a) but for the difference between the HIGH_K-UP_O and HIGH_K-DOWN_O experiments.

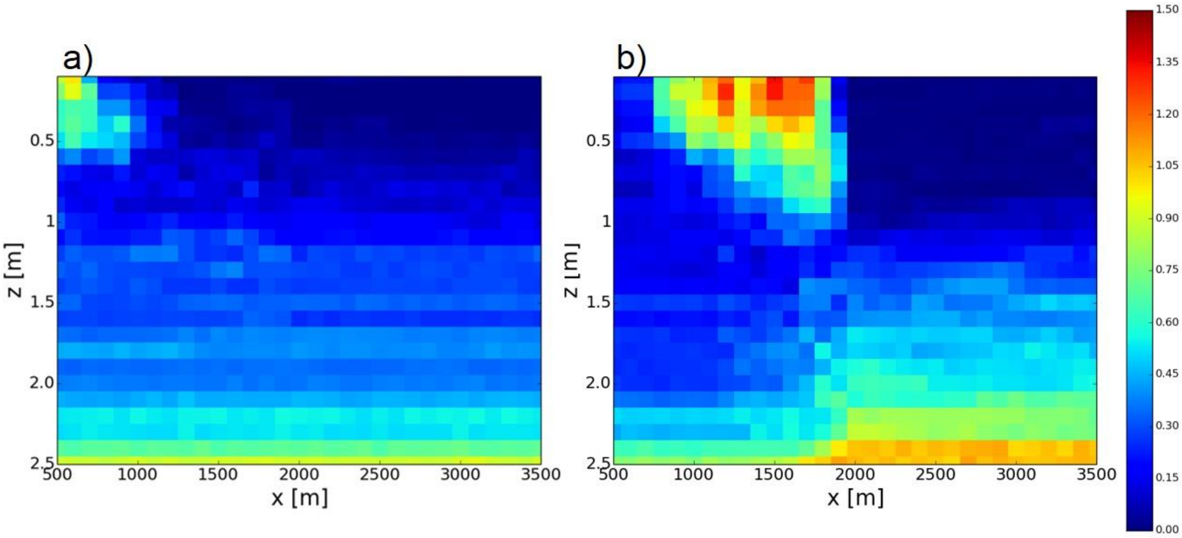

Figure 4. The Kullback-Leibler divergence of the NoDA experiment generated by (a) the LOW_K reference and (b) the HIGH_K reference at t = 130h (see also Figure 1b and 1d).

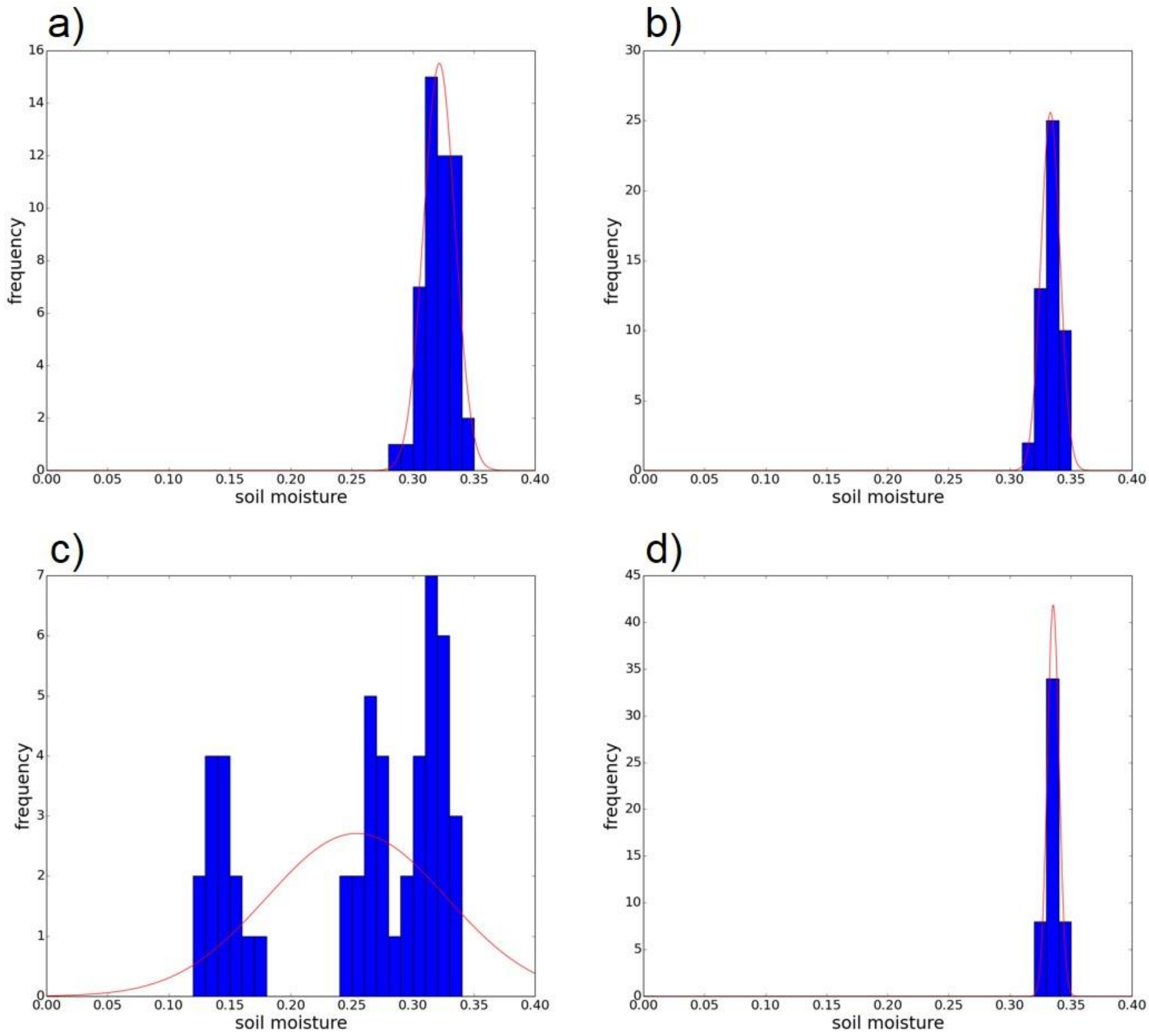

Figure 5. (a) The histogram (blue bars) of the volumetric soil moisture simulated by the NoDA experiment (see section 3) with the LOW_K reference at x=1500m, z=0.5m, and t=130h (see also Figure 4). Red line shows the Gaussian distribution with the mean and variance sampled by the ensemble. (b) same as (a) but at x=2500m, z=0.5m, and t=130h. (c) same as (a) but for the HIGH_K reference. (d) same as (c) but at x=2500m, z=0.5m, and t=130h.

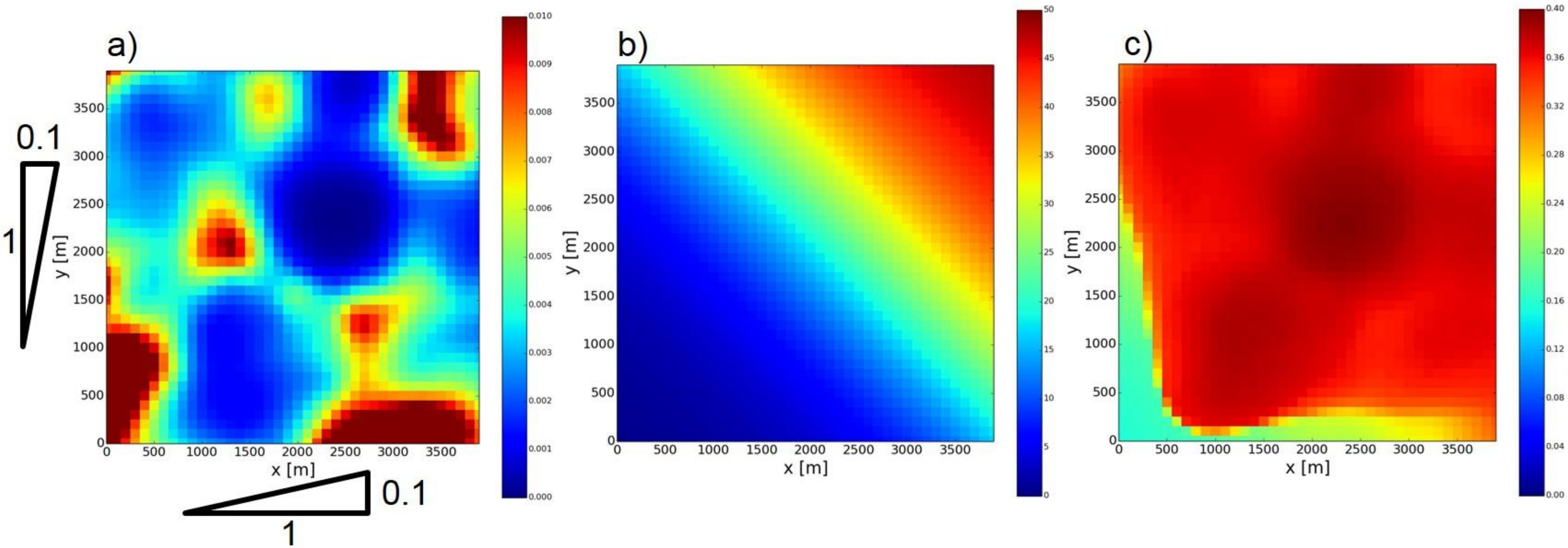

Figure 6. (a) Distribution of surface saturated hydraulic conductivity [m/h] in the synthetic reference. (b) Distribution of rainfall rate [mm/h] in the synthetic reference. (c) Surface volumetric soil moisture [m^3/m^3] at t = 5 [h] in the synthetic reference.

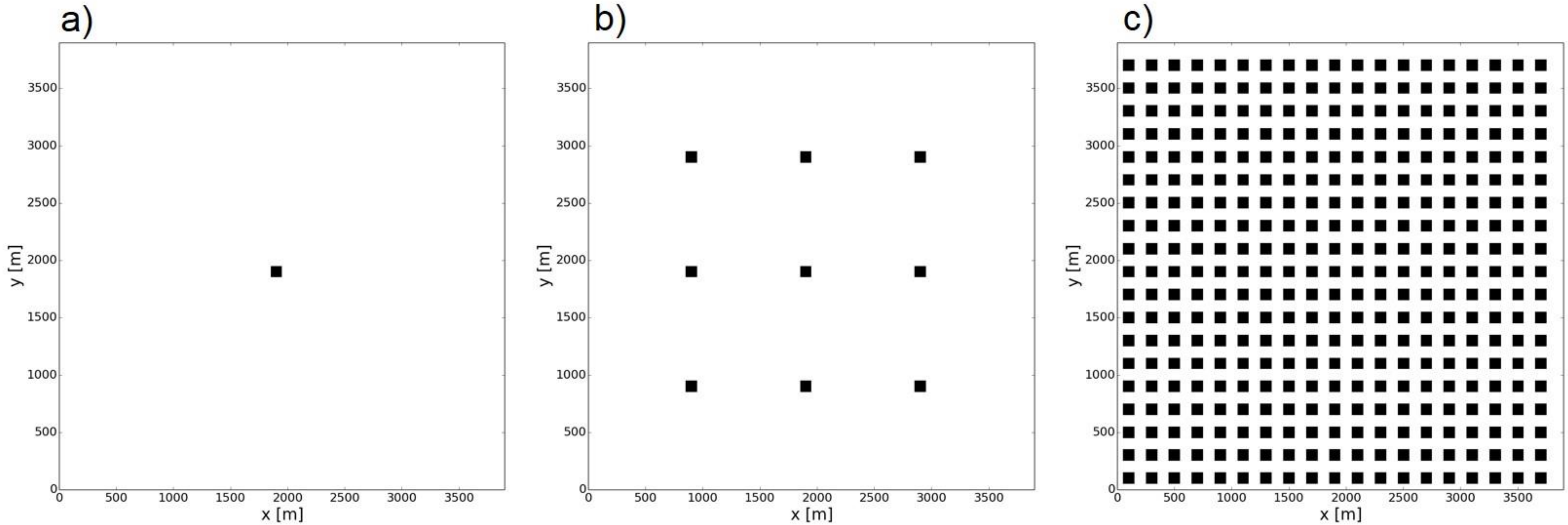

Figure 7. Observing networks. Black boxes are observed grids. (a) obs1, (b) obs9, (c) obs361 See also section 3.2.1.

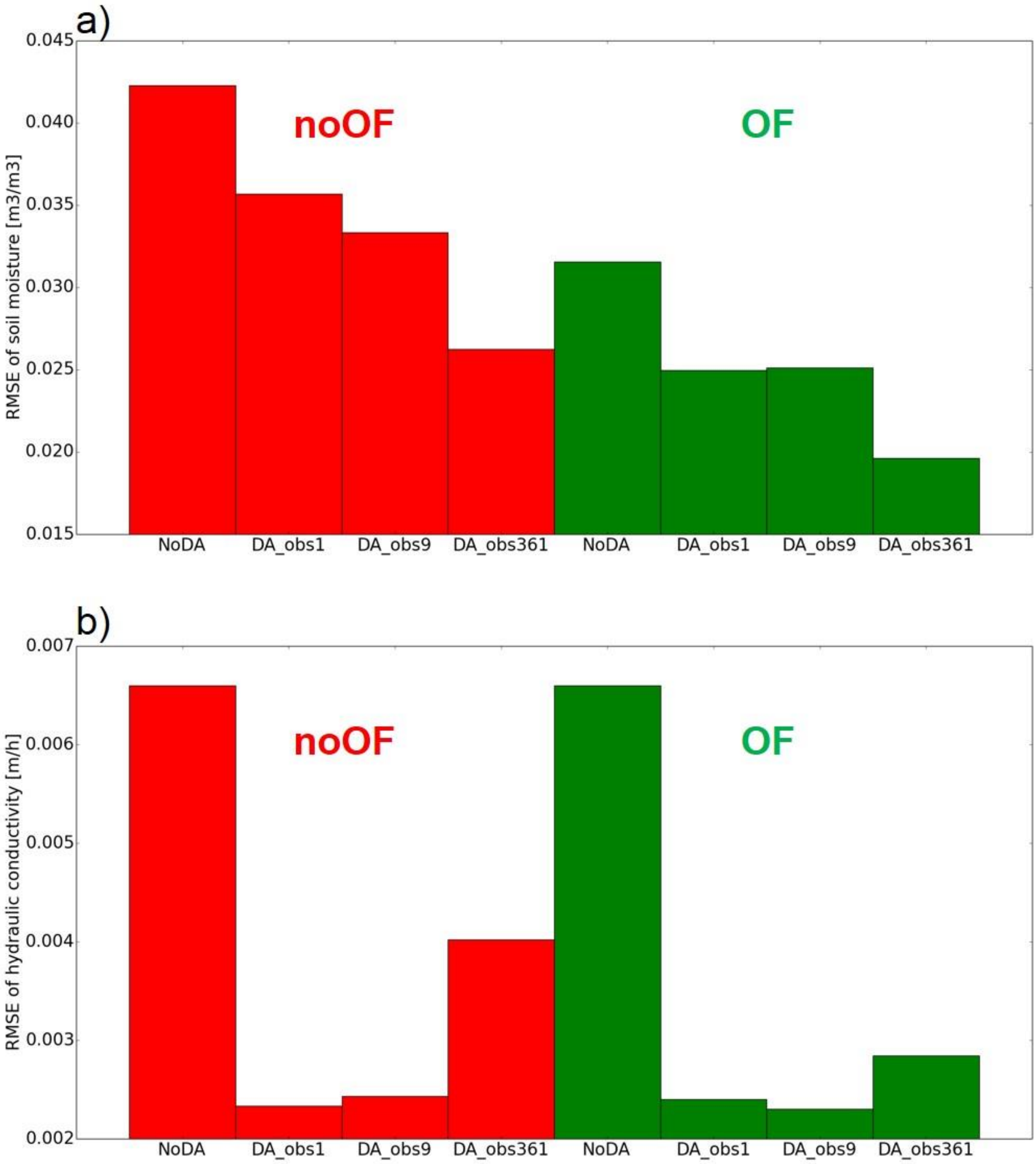

Figure 8. Time-mean RMSEs of the estimation of (a) soil moisture and (b) hydraulic conductivity. Red and green bars are results of the noOF and OF configuration, respectively (see section 3.2.1 and Table 2).

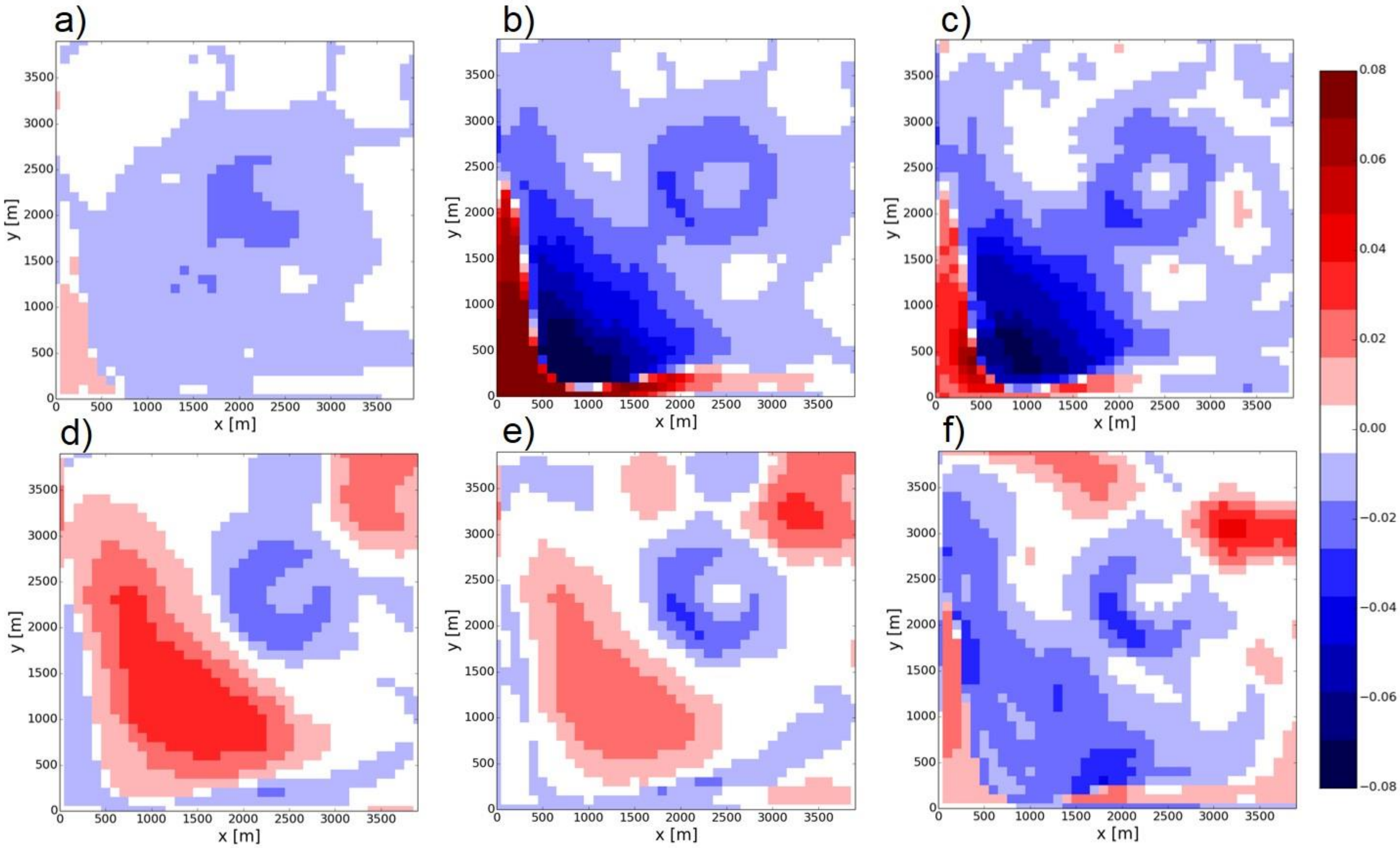

Figure 9. Differences of time-mean soil moisture RMSEs between the DA experiments and the OF_NoDA experiment. (a) OF_DA_obs1, (b) OF_DA_obs9 (c) OF_DA_obs361 (d) noOF_DA_obs1, (e) noOF_DA_obs9, (f) noOF_DA_obs361.

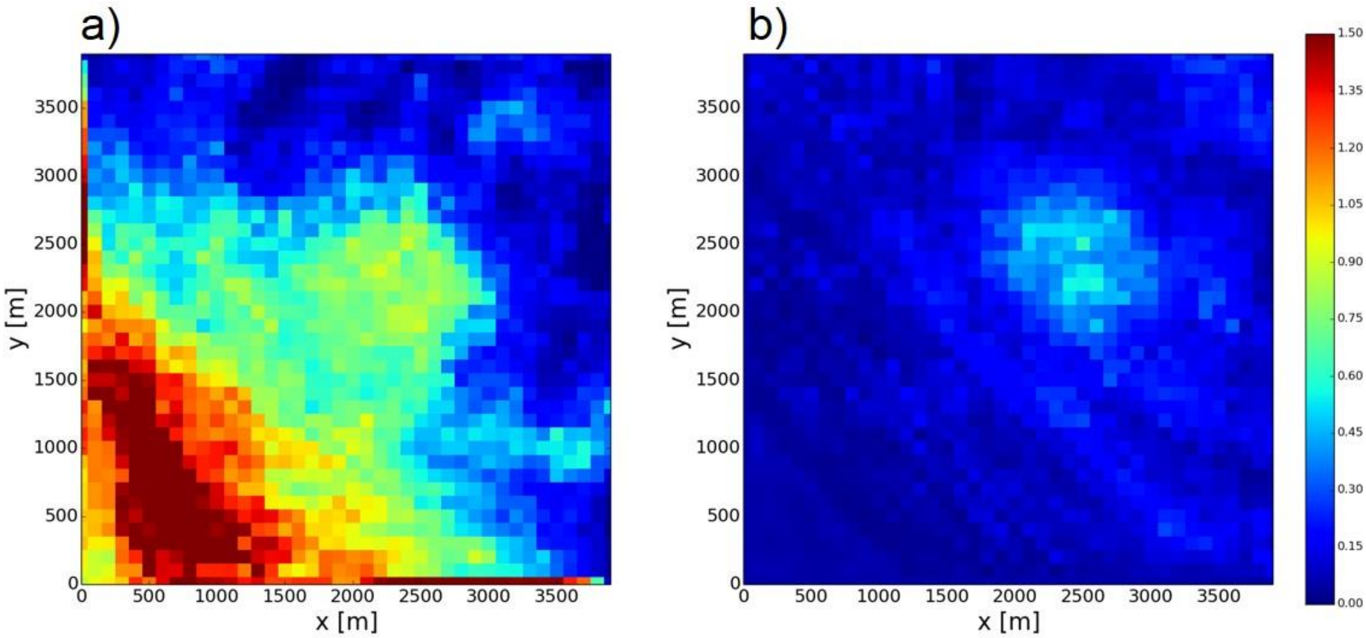

Figure 10. The Kullback-Leibler divergence of ensemble members generated by the (a) OF_NoDA and (b) noOF_NoDA experiments at t = 4 [h].

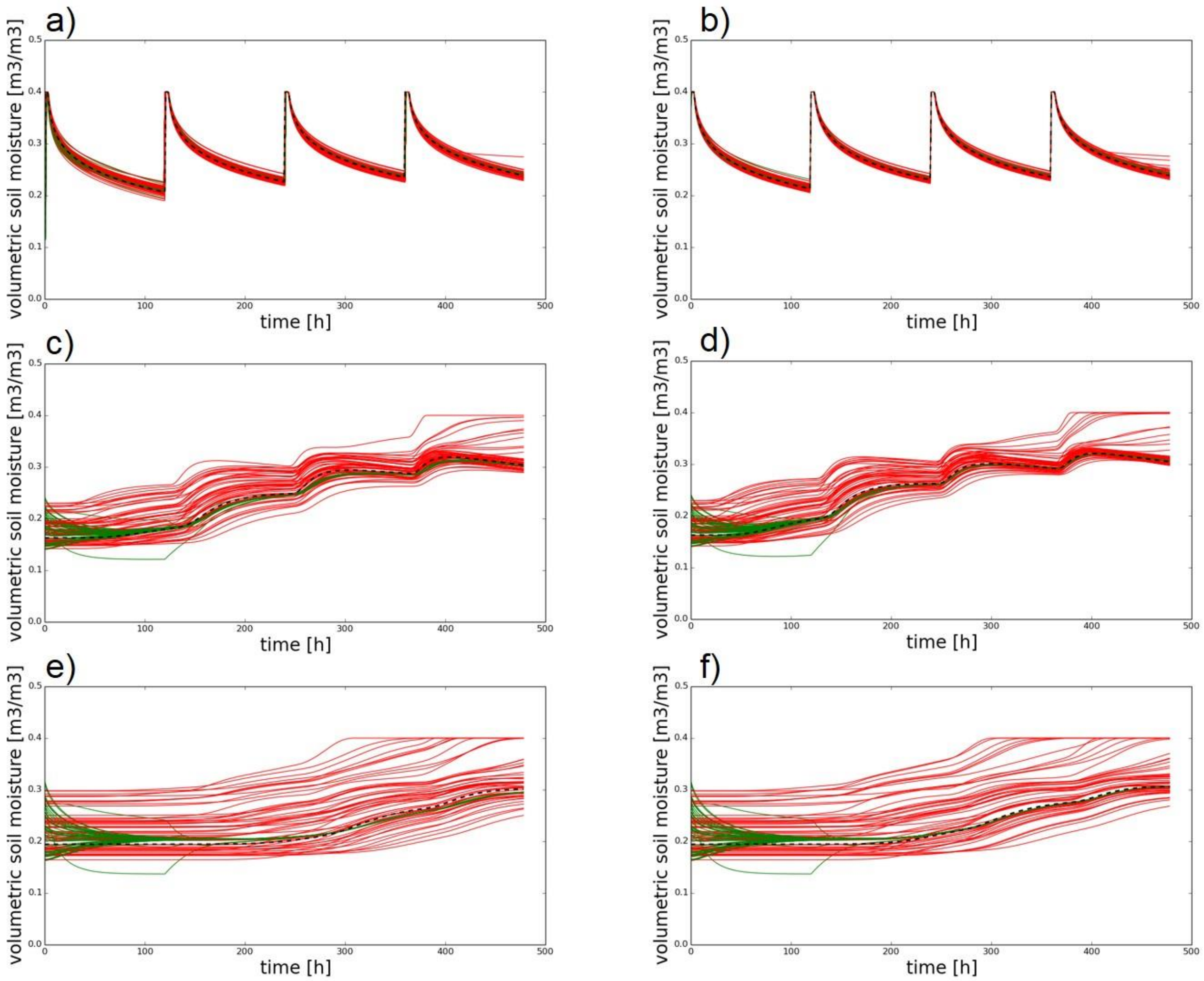

Figure S1. Time series of volumetric soil moisture simulated by the synthetic reference run (black dashed line), the NoDA experiment (red lines), and the DA experiment (green lines) in the LOW_K-UP_O experiment at a) x=1500m, z=0.05m; (b) x=2500m, z=0.05m; c) x=1500m, z=1.0m; (d) x=2500m, z=1.0m; e) x=1500m, z=1.5m; (f) x=2500m, z=1.5m.

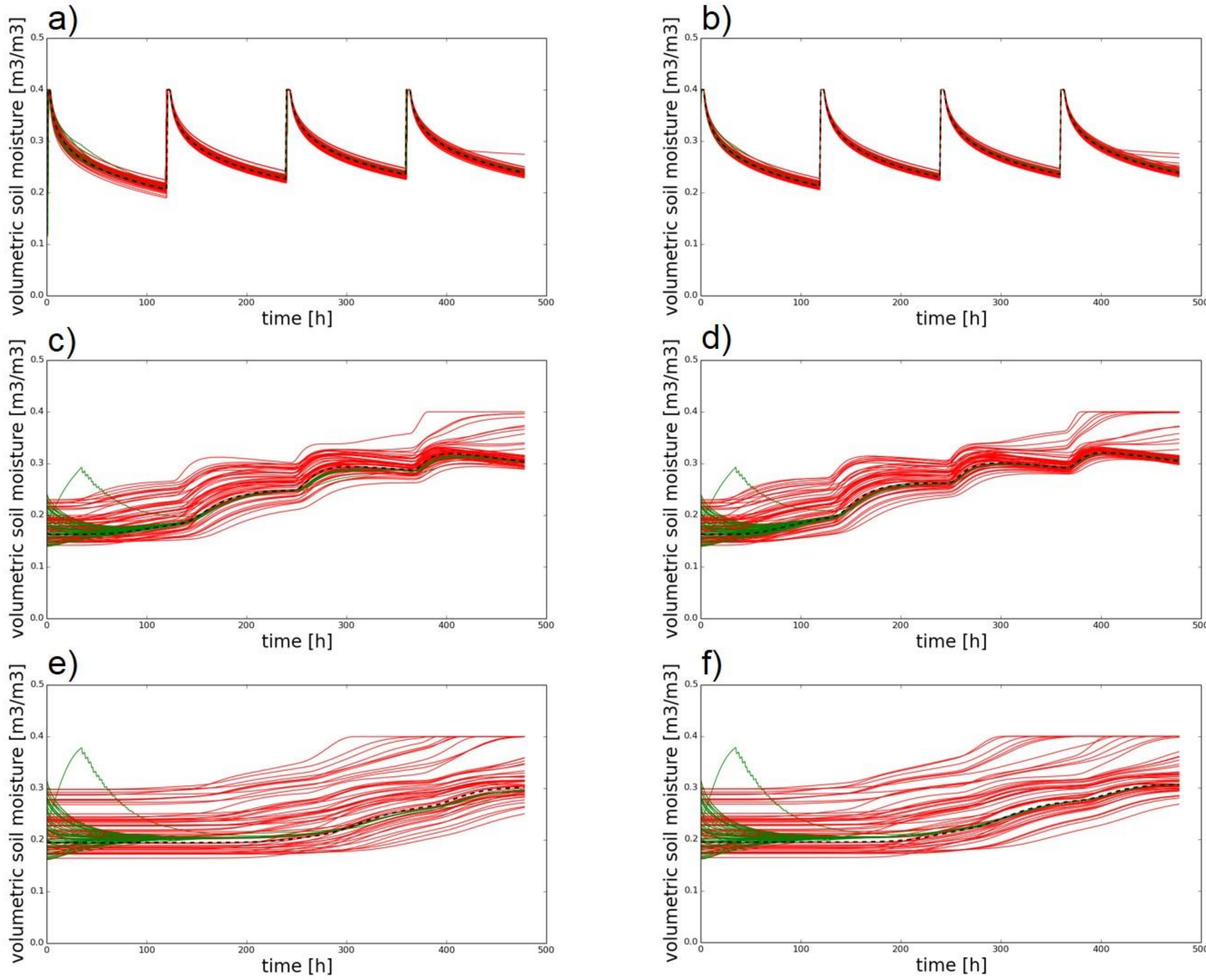

Figure S2. Same as Figure S1 but for the LOW_K-DOWN_O experiment.

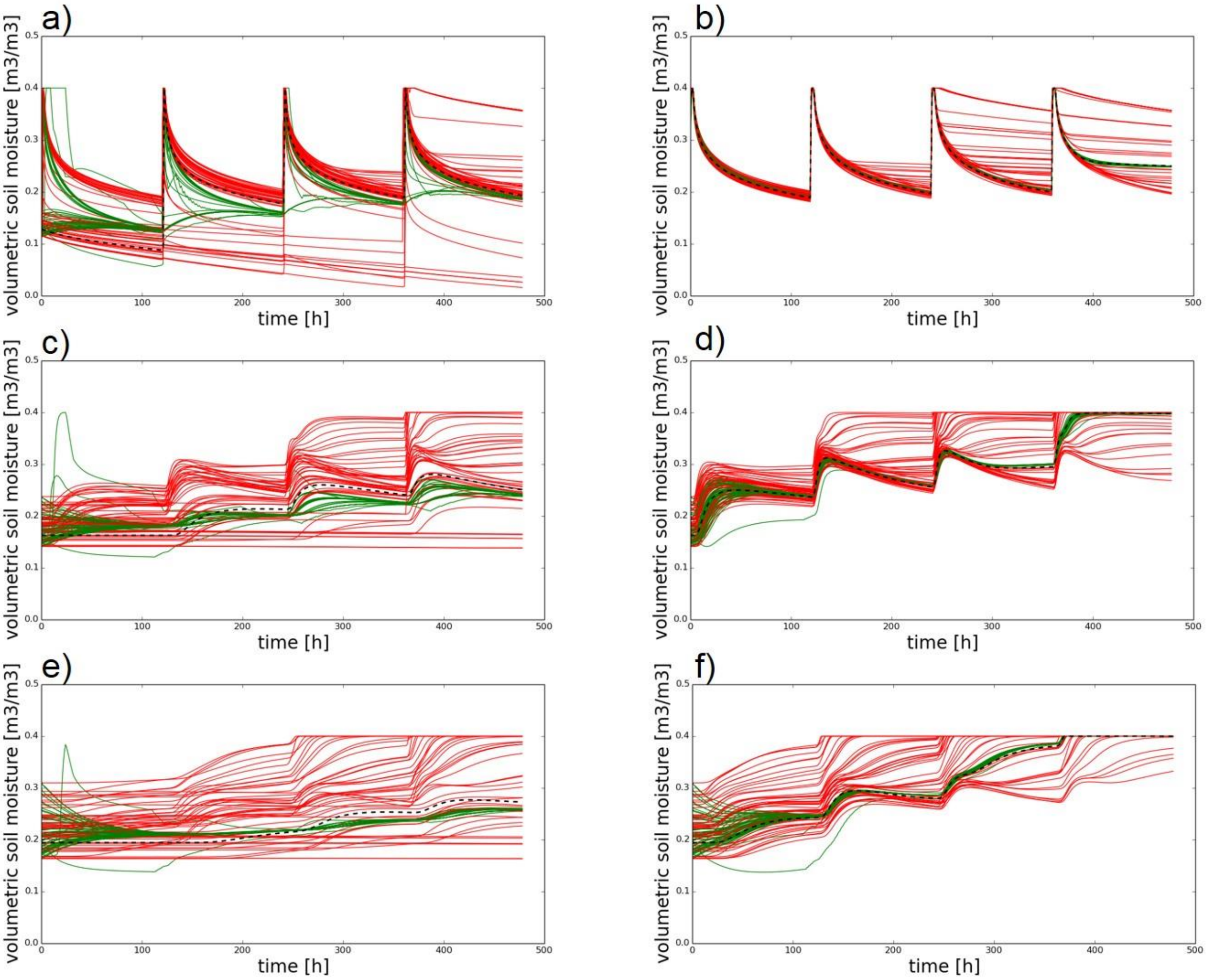

Figure S3. Same as Figure S1 but for the HIGH_K-UP_O experiment.

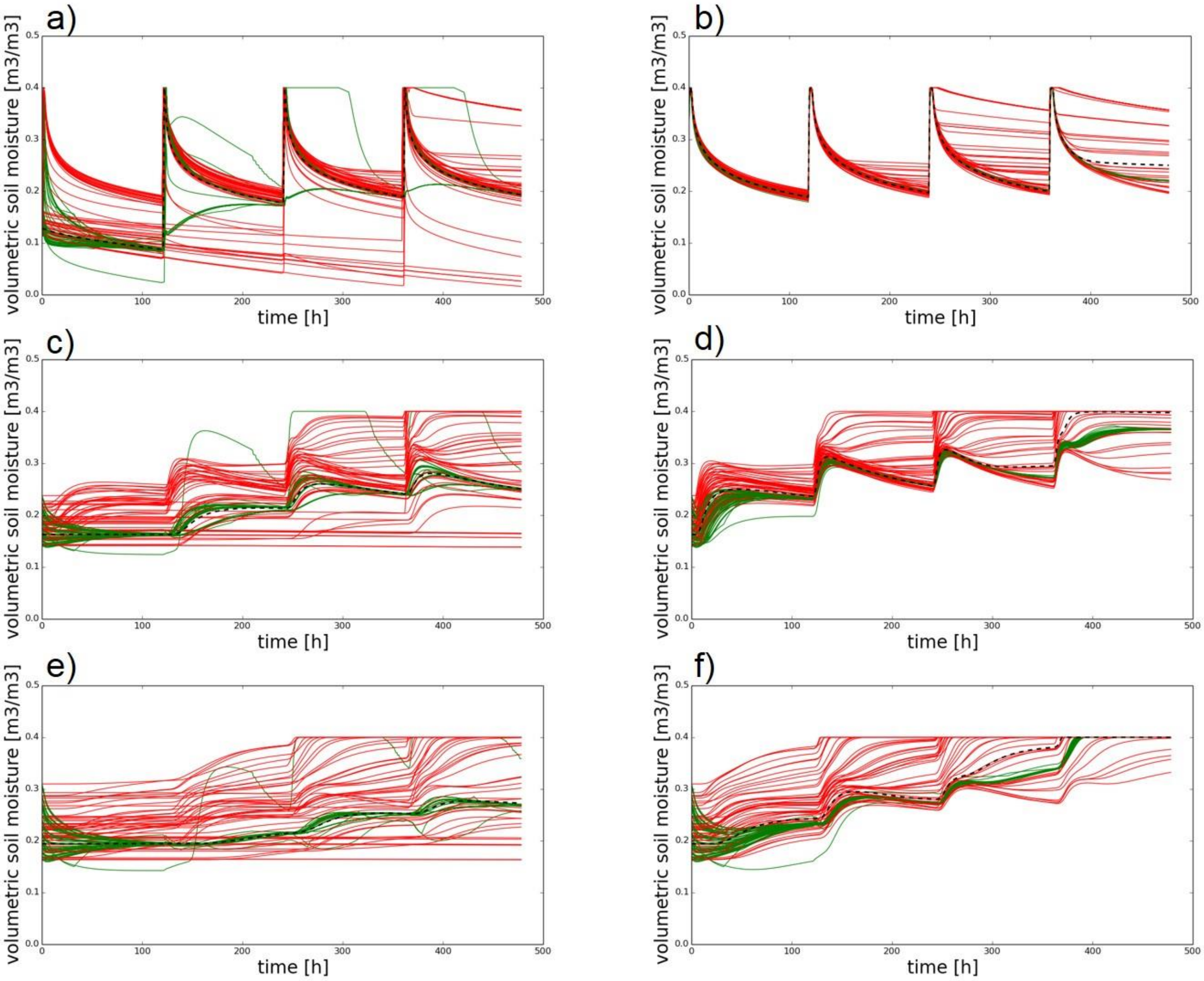

Figure S4. Same as Figure S1 but for the HIGH_K-DOWN_O experiment.

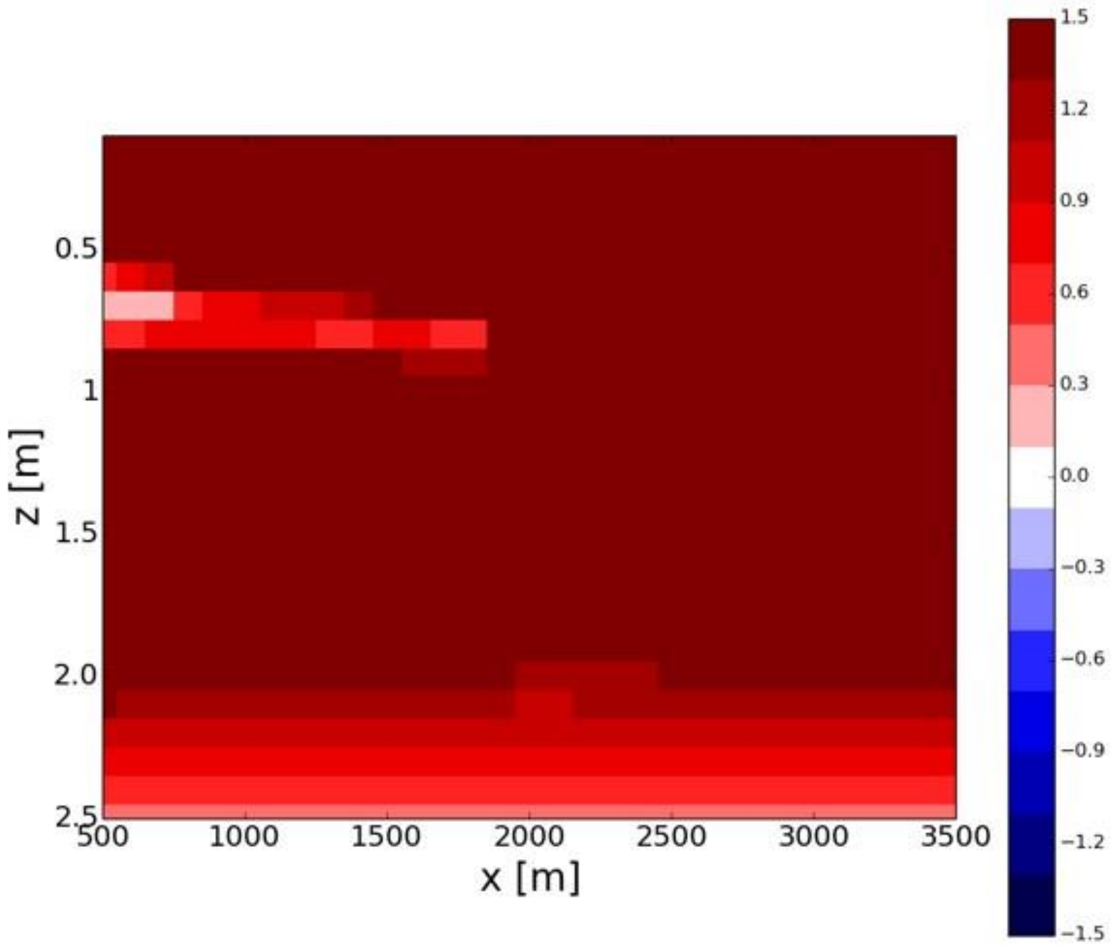

Figure S5. The improvement rates of the LOW_K-DOWN_O experiment where topography-driven surface flows are neglected in ParFlow.

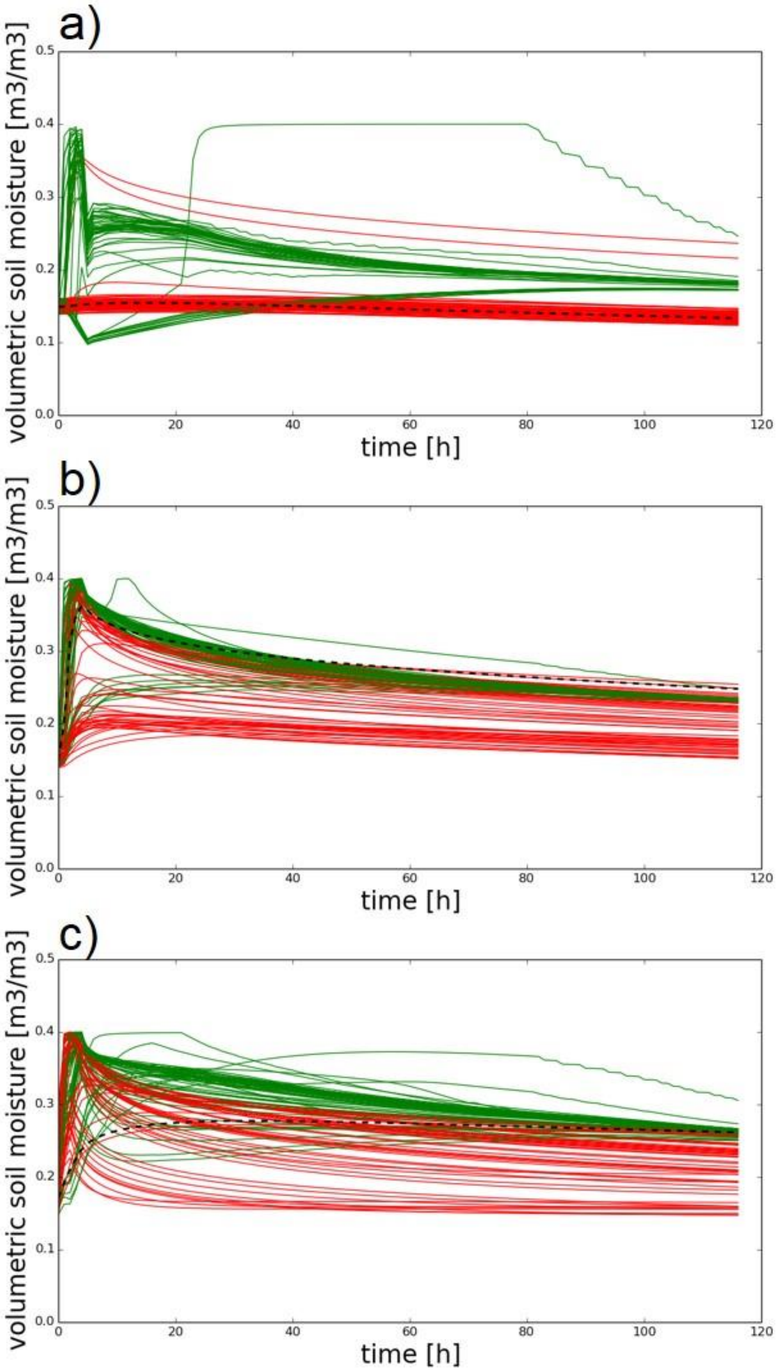

Figure S6. Time series of volumetric soil moisture simulated by the synthetic reference run (black dashed line), the OF_NoDA experiment (red lines), and the OF_DA_obs361 experiment (green lines) at a) x=200m, y=200m. z=0.15m; b) x=1200m, y=1200m, z=0.15m; c) x=2200m, y=2200m, z=0.15m.